

Review: grain boundary faceting–roughening phenomena

B. B. Straumal^{1,2,3,4} · O. A. Kogtenkova¹ · A. S. Gornakova¹ · V. G. Sursaeva¹ ·
B. Baretzky²

Received: 2 June 2015 / Accepted: 6 August 2015 / Published online: 19 August 2015
© Springer Science+Business Media New York 2015

Abstract Similar to free surfaces, the grain boundaries (GBs) in metals, semiconductors and insulators can contain flat (faceted) and curved (rough) portions. In the majority of cases, facets are parallel to the most densely packed planes of coincidence sites lattice formed by two lattices of abutting grains. Facets disappear with the increasing temperature (faceting–roughening transition) and the increasing angular distance from coincidence misorientation. The temperature of GB faceting–roughening transition T_R decreases with the increasing inverse density of coincidence sites Σ . In case of fixed Σ , T_R decreases with the decreasing density of coincidence sites in the GB plane.

The intersection line (ridge) between facets or between facets and curved (rough) portions of surfaces can be of first order (two different tangents in the contact point) or of second order (common tangent, continuous transitions). The rough (curved) portions of GB can also form the first-order rough-to-rough ridges (with two tangents). GB facets control the transition from normal to abnormal grain growth and strongly influence the GB migration, diffusion, wetting, fracture and electrical conductivity.

Introduction

The thermodynamics of surfaces and interfaces and in particular the concept of the surface free energy was introduced by Gibbs [1, 2]. He defined the surface free energy, σ , for a one-component material as the work dW required to create new surface area dA at a constant temperature and chemical potential, $\sigma = dW/dA$. For crystalline materials, this work depends on the atomistic structure of the surface. Therefore, in case of crystalline solids, σ is also orientation dependent. For multicomponent crystals, the surface free energy may also be a complex function of composition. The surface free energy also determines the conditions for existence of 2D-phases on free surfaces and interfaces as well as respective phase transformations between 2D-phases. Faceting–roughening phase transformations are of the most intriguing and fundamental in the areas of surface physics and chemistry.

Historically, they were also the oldest phenomena for the surface thermodynamics. One of the first fundamental problems of surface free energy was to find the shape of a crystal, where the total free energy would be minimal for the condition that the amount of solid matter is constant. The problem was mathematically formulated independently

✉ B. B. Straumal
straumal@mf.mpg.de; straumal@issp.ac.ru

O. A. Kogtenkova
koololga@issp.ac.ru

A. S. Gornakova
alenahas@issp.ac.ru

V. G. Sursaeva
sursaeva@issp.ac.ru

B. Baretzky
brigitte.baretzky@kit.edu

¹ Institute of Solid State Physics, Russian Academy of Sciences, Ac. Ossipyan Str. 2, 142432 Chernogolovka, Russia

² Karlsruhe Institute of Technology (KIT), Institute of Nanotechnology, Hermann-von-Helmholtz-Platz 1, 76344 Eggenstein-Leopoldshafen, Germany

³ Moscow Institute of Physics and Technology (State University), Institutskii per. 9, 141700 Dolgoprudny, Russia

⁴ Laboratory of Hybrid Nanomaterials, National University of Science and Technology «MISIS», Leninskii Prosp. 4, 119049 Moscow, Russia

by Gibbs [1, 2] and Curie [3] as a surface area integral over the orientation-dependent surface free energy. The solution was found by Wulff [4, 5] and generalized by Herring [6] and Landau and Lifshitz [7].

Wulff considered the case of slowly growing or slowly dissolving crystal [4, 5]. He considered the 2D sectional cuts through the crystal centre W in polar coordinates (Fig. 1) and supposed that the anisotropic function $\sigma(\theta)$ is known. $\sigma(\theta)$ is shown as the outer curve in Fig. 1. If $\sigma(\theta)$ is known, it is possible to determine the equilibrium crystal shape (ECS) $z(x)$ corresponding to the minimum of total free energy. The Wulff construction requires that a line is drawn from the origin W (Wulff point) to any point Q on $\sigma(\theta)$. One constructs the normal to the line WQ in the point Q . The inner envelope of all such normals (or planes for 3D case) gives the ECS $z(x)$. The anisotropic function $\sigma(\theta)$ is shown as the outer curve in Fig. 1 while the shape function $z(x)$ for ECS is plotted inside. The Wulff construction is completely equivalent to the Legendre transform [8]. If the anisotropic surface free energy $\sigma(\theta)$ contains minima (cusps), the ECS would have flat segments (facets). If these minima are deep enough, the facets intersect with each other forming ridges. The minima (cusps) in $\sigma(\theta)$ correspond to the low-energy densely packed planes in the crystal lattice. Less densely packed crystallographic planes possess shallower minima (see Fig. 1). If these secondary minima are not deep enough and are far away from the central point W , they cannot compete with deep primary minima and would not appear in ECS. If even the primary minima (cusps) are shallow, then the curved (rough) portions of surfaces appear and separate the primary facets. The intersection line (ridge) between facets or between

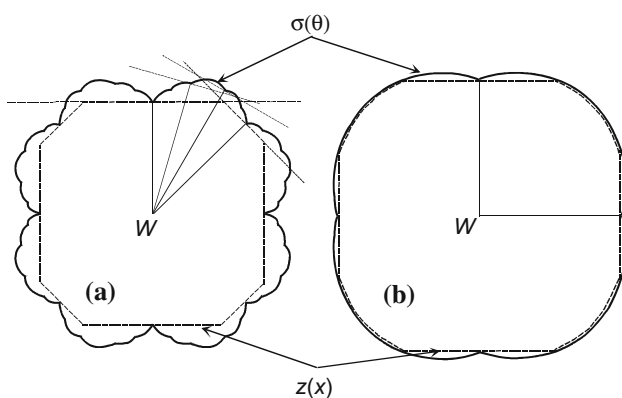


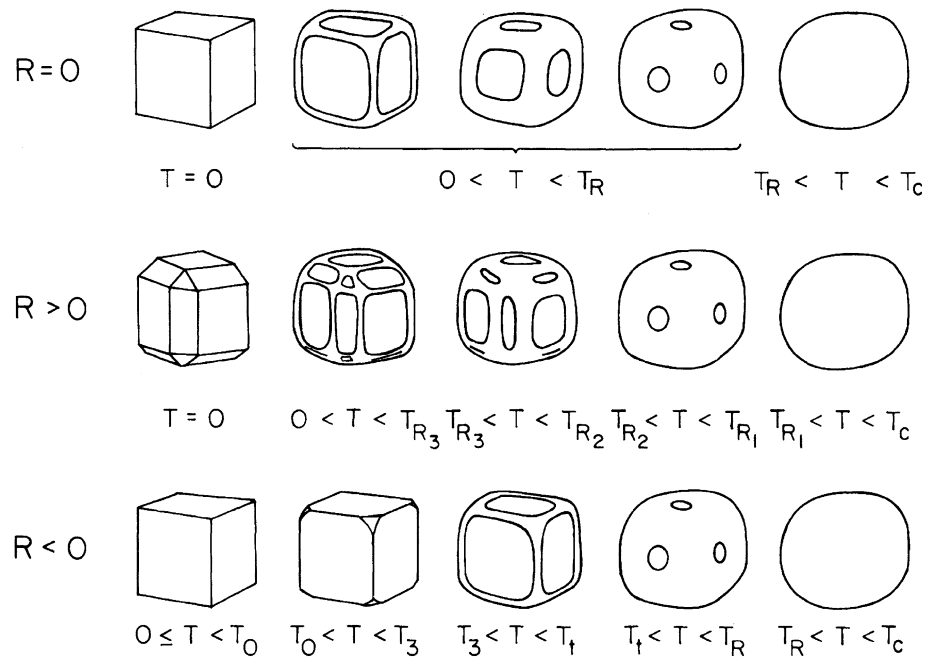
Fig. 1 Schematic illustrating the Wulff construction, connecting the anisotropic surface free energy $\sigma(\theta)$, outer curve, with the equilibrium crystal shape function $z(x)$, inner curve. W is the Wulff point. **a** $\sigma(\theta)$ contains six crystallographically different cusps, but ECS contains only two stable facets. Four facets corresponding to other cusps are metastable. **b** ECS contains only one kind of facets separated by curved (rough) portions of surface. Facets and rough surfaces contact along the first-order ridges

facets and curved (rough) portions of surfaces can be of first order (two different tangents in the contact point) or of second order (common tangent, continuous transitions). The rough (curved) portions of ECS can also form the first-order rough-to-rough ridges (with two tangents) [8–10].

The Wulff approach is very powerful and became quite useful in the materials science. Though the Wulff method for ECS in its original form was developed to explain “... rates of growth and dissolution of crystals” [4, 5], it was based on the assumption of constant volume. Later, similar approach was used in numerous papers for the analogous kinetic Wulff shape, which gives the limiting shape of a crystal growing outwardly under diffusion control (for the review see [11] and references therein). The methods of construction are the same, even though one is a minimization problem, and the other is a long-time solution of a first-order nonlinear partial differential equation. Moreover, the use of chemical potentials for solution thermodynamics is very similar to known vector formulations for surface thermodynamics and the method of characteristics which tracks the interfaces of growing crystals. Accordingly, the Wulff construction for ECSs has been modified to construct the so-called chemical Wulff phase shapes from solution free energies [12].

The shape of $\sigma(\theta)$ and, therefore, the shape of ECS can depend on temperature, pressure, impurities, etc. [13–15]. In order to relate expressions of continuum thermodynamics to the crystallographic features of atomic dimensions, one can calculate $\sigma(\theta)$ in the framework of the terrace–ledge–kink model of a surface [16–18]. The basic structural features of the terrace–ledge–kink model are steps of monatomic height, kinks, single adatoms and terrace vacancies. Steps and kinks may be intrinsic crystallographic defects as well as thermally excited defects at elevated temperature. In the latter case, the increasing temperature increases surface roughness. A first systematic study of step interactions on model single crystal surfaces gave the expression for the surface free energy which depends on the (1) surface free energy of a flat terrace (facet), (2) the local step density of the surface, (3) the free energy of an isolated step, and (4) the step interaction energy [19]. The temperature dependence of ECS has also been calculated for 3D Ising models with the nearest and the next-nearest neighbour atomic interactions (the so called solid-on-solid models) [20–23]. The models of this type predict the fully faceted crystals at $T = 0$ (with one, two or three crystallographically different facets, depending on the atomic interactions). These facets shrink with the increasing temperature, and rounded vicinal regions appear (Fig. 2). Each type of facet vanishes at a characteristic roughening temperature T_R . According to theory [24, 25], the roughening phase transition is of the Berezinskii–Kosterlitz–Thouless type [26–28].

Fig. 2 Different scenarios of surface roughening with the increasing temperature. Reproduced from [22] with permission from APS



Faceting of grain boundaries

Special and general grain boundaries

High-angle grain boundaries (GBs) are those with misorientation angle θ above 15° . They cannot be described as an array of lattice dislocations since at high θ , the dislocation cores merge. In case of free surfaces, the minima (cusps) in $\sigma(\theta)$ and the planes in ECS correspond to the low-energy densely packed planes in the crystal lattice. In case of GBs, the orientation of plane facets is determined by two crystalline lattices of abutting grains. Consider two interpenetrating crystalline lattices 1 and 2 and start to rotate them around one common lattice position. At certain misorientations θ_Σ called coincidence misorientations, a part of the lattice sites of the lattice 1 coincide with the lattice sites of the lattice 2 forming a coincidence sites lattice (CSL) [29–31]. This fact was first observed by Kronberg and Wilson [32]. CSL is characterized by a parameter Σ (Σ is the inverse density of coincidence sites). For example, $\Sigma = 5$ means that each fifth position of lattices 1 and 2 coincides with each other. CSL is the superlattice for lattices 1 and 2. Later all possible CSLs for densely packed lattices were numerically predicted and analysed [29]. Exactly at θ_Σ , GBs have a very perfect periodic structure. These coincidence GBs have low energy σ_{GB} , migration rate, diffusion permeability, high strength and other extreme properties. The coincidence GBs also tend to facet. In other words, a curved GB breaks into an array of flat segments [33]. These segments are usually parallel to the CSL planes densely packed with coincidence sites. Here we observe the

similarity with facets on free surfaces which are parallel to the densely packed planes of crystal lattice. Strictly speaking, a CSL exists only exactly at θ_Σ . Any low deviation, $\Delta\theta = |\theta - \theta_\Sigma|$ destroys the geometrical coincidence of lattice sites. However, physically a GB tends to conserve its low-energy structure up to certain $\Delta\theta$. The structure of such (special) GBs consists of portions of perfectly coincident lattices separated by the intrinsic GB dislocations (IGBDs) [34]. The IGBDs have a Burgers vector b_Σ which is shorter than that of lattice dislocations b : $b_\Sigma = b \Sigma^{-2}$. The Burgers vectors b_Σ are elementary vectors of the displacement shift lattice (DSC) introduced by Bollmann [35]. DSC is a reciprocal lattice of CSL.

Here we have to underline that there is no direct connection between coincidence and GB energy. In the early works, the following geometric criteria were proposed for the low GB energy: (i) low reciprocal volume density of coincidence sites Σ [32]; (ii) high planar density of coincidence sites, Γ [36]; (iii) high Γ at constant interplanar spacing, d [37]; (iv) large interplanar spacing, d [37] and (v) high density of locked-in rows of atoms [38]. It has been shown that the prediction power of these simple criteria is highly limited [39–44]. In metals, low grain boundary energy is associated with dense arrays of closely packed polyhedral groups of atoms in which the atomic coordination number is as close as possible to that of the perfect crystal [45]. Low grain boundary energy in ionic crystals is always associated with the absence of the nearest-neighbour ions of the same sign [37]. Not only CSL GBs can possess low energy and, therefore, tend to facet [44]. Prominent example represent the so-called 9R low-

energy non-CSL facets which can be easily observed as asymmetric $\Sigma 3$ twin GBs in Cu, Ag and other face-centred cubic (fcc) metals [46–49].

It has been demonstrated that the special GBs conserve their special structure and properties up to a certain critical misorientation $\Delta\theta_c$ and temperature T_c [50]. In the “Temperature–Misorientation” coordinates, the areas of existence of GBs with special structure and properties have a shape of domes symmetric with respect to θ_Σ (Fig. 3). T_c decreases parabolically, and $\Delta\theta_c$ decreases exponentially with the increasing Σ (Figs. 4, 5) [51]. In other words, with the decreasing temperature, more and more GBs with higher and higher Σ possess special structure and properties. The physical reason for such behaviour is the GB faceting–roughening phase transformation similar to those for free surfaces [52–54]. The energy of individual steps in a flat surface facet decreases with the increasing temperature. At certain temperature T_R , step energy becomes zero. If $T_R < T_m$ (T_m is the melting temperature), the flat facet cannot be stable above T_R due to the spontaneous formation of step arrays and becomes rough (roughening transition) [22, 55]. It has been predicted theoretically that T_R is lower for the facets with higher step energy (i.e. for the facets less densely packed with lattice sites) [55, 56]. Experimentally a sequence of three roughening transitions for different surface facets at different T_R has been observed only in solid helium [57]. Potential GB Wulff

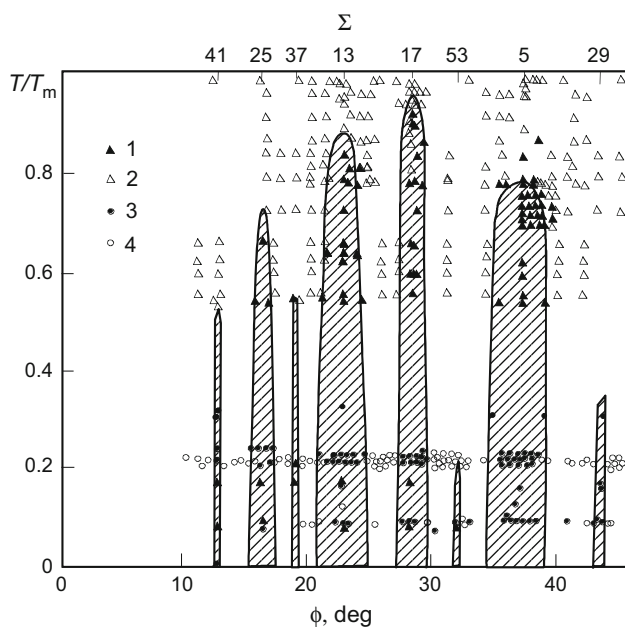


Fig. 3 Regions of existence of special and non-special (general) grain boundaries with (100) misorientation axis. 1 GBs with special properties. 2 GBs with non-special properties. 3 GBs with special structure. 4 GBs with non-special structure. Reproduced from [51] with permission from Elsevier

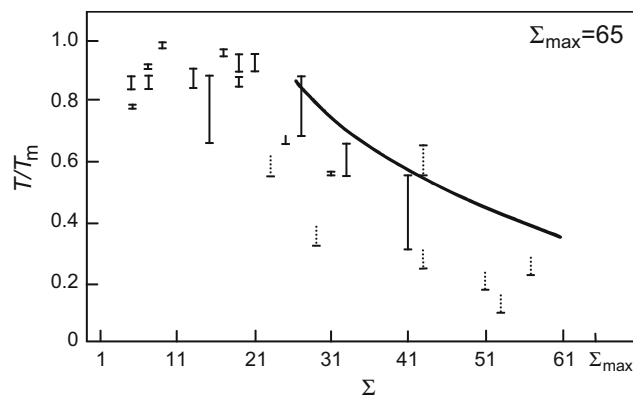


Fig. 4 Dependence of the transition temperature from special to general GBs on inverse density of coincidence sites Σ . Reproduced from [51] with permission from Elsevier

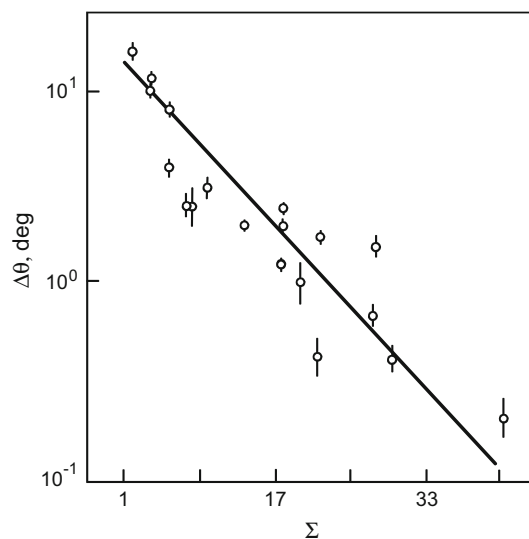


Fig. 5 Dependence of the angular interval of existence of special GBs on inverse density of coincidence sites Σ . Reproduced from [51] with permission from Elsevier

shapes for various Σ for fully faceted GBs at $T = 0$ were analysed in [58].

Faceting–roughening of twin ($\Sigma = 3$) grain boundaries in copper

In metals having fcc lattice with low-to-medium stacking fault energy (SFE), the population of special (CSL) boundaries is dominated by the $\Sigma 3$ and related $\Sigma 3^2$ ($\Sigma 9$) and $\Sigma 3^3$ ($\Sigma 27$) GBs [44, 59, 60]. For example, the coherent twin typically accounts for 10–50 % of the grain boundary area in an annealed fcc polycrystal [61]. It is mainly due to the fact that the coherent twin energy is very low in fcc metals. Thus, the coherent twin energy in fcc Ni is reported as 0.064 J/m^2 , or 0.058 of the average boundary energy

[42]. In body-centred cubic (bcc) metals, the energy of coherent twins is not as low. Therefore, for bcc Fe, the coherent twin has the energy of 0.26 J/m^2 , or 0.23 of the average energy [44]. As a result, the coherent twin population in ferritic steels is 3 % or less [62, 63]. Nevertheless, the coherent twins dominate in the CSL GBs population also in bcc metals ([44] and references therein). Twins play a special role also in metals with hexagonal lattice [64] and semiconductors [65]. Therefore, we illustrate numerous faceting–roughening phenomena using twin GBs.

CSL plays for GBs a role similar to that of crystal lattice for the free surfaces. Therefore, one can expect that with the decreasing temperature, the new GB facets with the decreasing density of coincidence sites can appear [66] in a similar manner in which the GBs with high Σ become special at low temperature [51]. Such phenomenon has been indeed observed in [67]. The faceting of a tube-like $\Sigma = 3$ CSL tilt grain boundary in Cu bicrystals has been studied in the temperature interval from 0.5 to 0.95 of the copper melting temperature T_m ($T_m = 1356 \text{ K}$) [67]. In case of tubular samples, GB is slowly moving towards the sample axis due to the capillary reasons. It has been shown that the slowly growing or shrinking crystals obtain shape which is very close to the ECS [11, 12]. Moreover, the difference between energies of various facets is usually very low and, therefore, it cannot kinetically ensure the equilibration of GB shape towards ECS. In this case, the slow capillary-driven GB migration permits GB to get its equilibrium shape. Similar method was used to study the “special-to-general” GB transformations for $\Sigma 17$ GBs in tin [50]. In case of quick GB migration, the facets are no longer in equilibrium and are defined by kinetic differences (see the “Grain boundary migration, diffusion and fracture” section). In other cases, a GB is not tubular, and a different kind of constraint is imposed on a GB, such as a requirement to preserve certain average inclination. In this case, the stability of initially planar GB is determined by the inverse sigma-plot construction which, generally speaking, is different from the Wulff construction [46–49].

The grains of the bicrystals formed the coincidence site lattice with inverse density of coincidence sites $\Sigma = 3$ [67]. Three is the lowest possible value of Σ for CSLs between two fcc lattices. In the whole studied temperature interval, the facets of $\Sigma 3$ GBs intersect each other (Fig. 6a, b). The rounded (rough) edges between facets were not observed.

Above $0.8 T_m$, only two different GB facets were observed, namely the most closely packed $(100)_{\text{CSL}}$ and the so-called non-CSL $9R$ facet. $(100)_{\text{CSL}}$ facet is also called symmetric twin GB where the most closely packed planes $\{111\}_1$ and $\{111\}_2$ of both fcc grains are parallel to each other. At high temperatures, the twin plates in Cu are not rectangular unlike those in Au [40]. The facets at the end of twin plates form an angle of $\varphi = 82^\circ$ with $(100)_{\text{CSL}}$ plane

(Fig. 6a). φ is the inclination angle between actual GB plane and lowest-energy GB position at $\varphi = 0^\circ$ (symmetric twin GB in our case). The 82° facet does not correspond to any low-index CSL plane. The minimum of GB energy $\sigma_{\text{GB}}(\varphi)$ at 82° is due to the existence of thin GB layer with the so-called $9R$ structure forming a plate of bcc GB phase in the fcc matrix [46–49]. Another non-CSL facets were also theoretically predicted [68]. The $(100)_{\text{CSL}}/82^\circ 9R$ edges of the twin plates are sharp. By decreasing the temperature, new facets appear in ECS of the $\Sigma 3$ GB. The results are given in Figs. 2 and 4. These additional facets are $(010)_{\text{CSL}}$, $(110)_{\text{CSL}}$, $(120)_{\text{CSL}}$ and $(130)_{\text{CSL}}$. All of them are less densely packed CSL facets than $(100)_{\text{CSL}}$. At $T = 673 \text{ K} = 0.5 T_m$, six crystallographically different facets exist simultaneously for $\Sigma 3$ GB. All observed edges between the facets are sharp. Hence, the new facets appear not at the rough rounded parts of the GB, as observed for surface facets in Pb, Au or He [57, 69–71], but at the sharp edges between existing facets. It means that the temperature T_{Rf} when a less densely packed CSL facet really appears in ECS is lower than true roughening temperature T_{R} for this facet. This feature is illustrated schematically in Fig. 7 for the $(010)_{\text{CSL}}$, $(110)_{\text{CSL}}$, $(120)_{\text{CSL}}$ and $(130)_{\text{CSL}}$ facets. At T_{R} , the cusp in $\sigma(\mathbf{m})$ appears but it is too shallow to contribute to ECS, and the $(130)_{\text{CSL}}$ facet is metastable. Only when temperature decreases, the cusp becomes deep enough, and the metastable facet becomes stable and appears at T_{Rf} in ECS. At T_{Rf} , the plane normal to the radius-vector at the respective cusp in $\sigma(\mathbf{m})$ for $(hkl)_{\text{CSL}}$ facet touches $z(\mathbf{h})$, and $(hkl)_{\text{CSL}}$ facet appears in the equilibrium shape. If we suppose that $\sigma_{hkl}/\sigma_{(100)}$ remains unchanged at low temperatures, we can estimate the values $\sigma_{hkl}/\sigma_{(100)}$ for the less densely packed $(hkl)_{\text{CSL}}$ facets from this construction in Fig. 3.

According to theory [24, 25], the roughening transition is of the Berezinskii–Kosterlitz–Thouless type [26–28], and should occur at the roughening temperature T_{R} , given by

$$k T_{\text{R}} = 2\gamma_{\text{R}} d^2 / \pi, \quad (1)$$

where k is Boltzmann’s constant, γ_{R} is the interface stiffness at T_{R} , and d is the interplanar spacing, i.e. the distance between subsequent crystalline planes, measured in the direction normal to the surface. Neglecting the anisotropy of interfacial tension [24, 25] one can substitute the interface stiffness γ_{R} by σ_{GB} . In case of GB, one has to use the displacement shift complete lattice [29] and grain boundary shifts lattice [72] to define d being the height of the elementary step for each CSL facet. If one uses for the $\sigma_{(100)}$ the values of SFE in Cu ($5.5 \times 10^{-4} \text{ J/m}^2$ [73] or $7.8 \times 10^{-4} \text{ J/m}^2$ [74]) one obtains $T_{\text{R}} = 1.4\text{--}1.9 T_m$ for the $(100)_{\text{CSL}}$ facet in Cu. Using the measured value $\sigma_{9R}/$

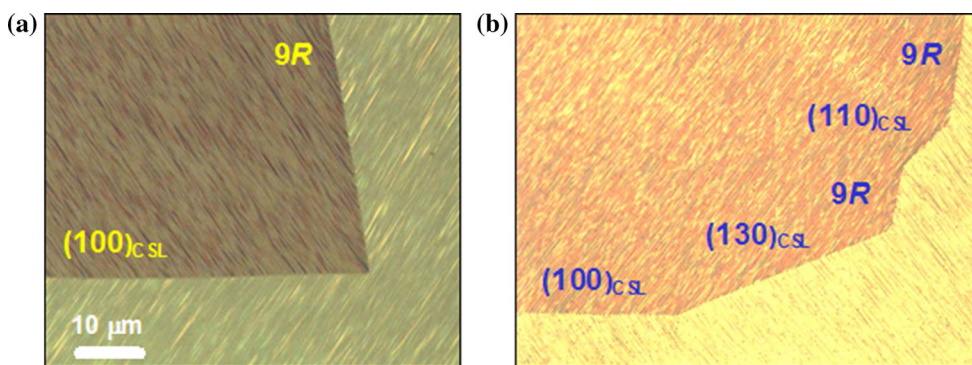


Fig. 6 Light micrographs of the faceted $\Sigma 3$ GB in Cu bicrystal at **a** 800 °C and **b** 400 °C

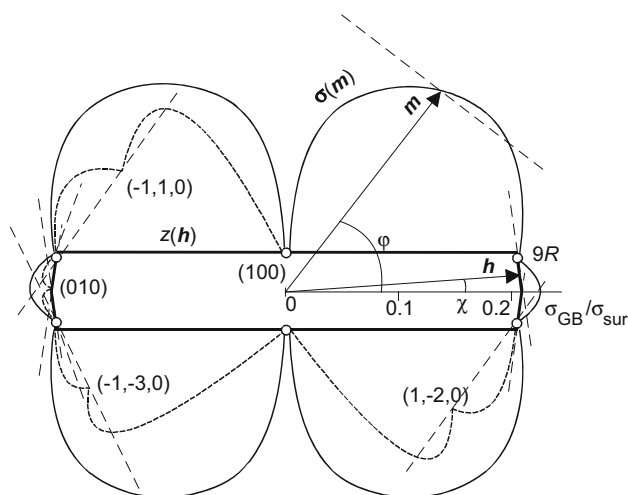


Fig. 7 Wulff–Herring energy $\sigma(m)$ (thin solid line) and resulting ECS $z(h)$ (thick solid line) in plane section normal to the $\{110\}$ tilt axis for the $\Sigma 3$ GBs in Cu at 1293 K. Open circles represent the GB energy σ_{GB} for the $(100)_{CSL}$, and $9R$ facets measured with the aid of atomic force microscopy (AFM). φ and χ are angular variables which measure interfacial orientation (m) and crystal shape (h), respectively. The cusps (dashed thin curves) for the $(010)_{CSL}$, $(110)_{CSL}$, $(120)_{CSL}$ and $(130)_{CSL}$ facets with normal planes touching the $z(h)$ are also shown. Reproduced from [67] with permission from Elsevier

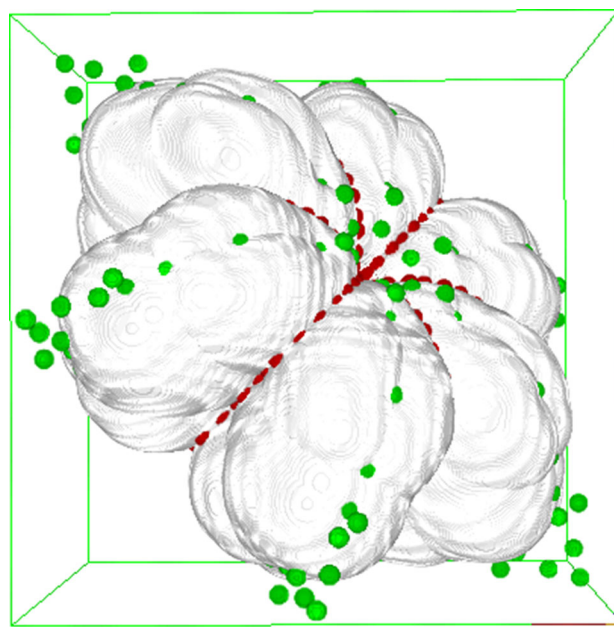


Fig. 8 Three-dimensional Wulff diagram for $\Sigma 3$ GBs in Cu obtained by using the experimental data from [67]. Reproduced from [75] with permission from Trans Tech Publications

$\sigma_{(100)} = 6$ (Fig. 7) one obtains from Eq. (1) $T_R = 0.9–1.3 T_m$ for the $9R$ facet. It reflects well the fact that $(100)_{CSL}$ and $9R$ facets remain in ECS of $\Sigma = 3$ GB in Cu up to the melting temperature T_m . In other words, the Eq. (1) derived for surface roughening basing on the Berezinskii–Kosterlitz–Thouless type theory [24–28] is applicable also for GBs. Therefore, using the temperature of actual appearance of each facet T_{Rf} instead of T_R in (1), one can estimate again the $\sigma_{hkl}/\sigma_{(100)}$ values for the less densely packed $(hkl)_{CSL}$ facets. The discrepancies with $\sigma_{hkl}/\sigma_{(100)}$ estimations obtained from Wulff-plot can be due to the fact that T_{Rf} is lower than actual (and unknown) T_R .

In Fig. 8, the 3D phase diagram for the $\Sigma 3$ twin GBs in Cu is shown in the “Relative temperature T/T_m –misorientation angle θ –inclination angle φ ” coordinates (T being

the annealing temperature, T_m being the melting temperature of Cu) [75]. Zero value of inclination angle $\varphi = 0$ corresponds to the symmetric twin GB. There are a huge number of papers where the faceting of symmetric twins in pure Cu was observed up to the melting temperature (some of these papers are [66, 67, 77–82]). It means that the roughening does not take place for the symmetric $\Sigma 3$ twin GBs up to the melting point (Fig. 1a). The misorientation interval $\Delta\theta = |\theta - \theta_{\Sigma 3}|$ where the $\Sigma 3$ twin GBs remain faceted is finite and very broad [67]. In case of copper, the direct evidence exists for the faceting of symmetric $\Sigma 3$ twin GBs up to $\Delta\theta = 2^\circ$. The indirect evidence from rotating single crystal balls experiments gives the $\Delta\theta > 4^\circ$ [83]. It has to be underlined that the phase diagram in Fig. 7 concerns only high-purity copper, since the addition

of impurities can drastically change the faceting behaviour of $\Sigma 3$ twin GBs in copper [78–80]. The inclination dependence for $\Sigma 11$ tilt GBs in Cu was obtained in [81].

The (T, φ) section of interfacial stability diagram for $\Sigma 3$ {110} tilt GBs in Cu [67] shown in Fig. 9 is very similar to the (T, θ) interfacial stability diagram for {100} tilt GBs shown in Fig. 3 [67]. The width $\Delta\theta$ and height T_c of the stability “domes” at θ_{Σ} for special GBs with different misorientations θ decreases with the increasing Σ (i.e. with the decreasing bulk density of coincidence sites). The width $\Delta\varphi$ and height T_c of the stability “domes” for different inclinations decreases with the decreasing plane density of coincidence sites.

Faceting–roughening of twin grain boundaries in other materials

For the construction of the “ T – θ ”, the interfacial stability diagram for {100} tilt GBs (Fig. 3) and “ T_c – Σ ” and “ $\Delta\theta$ – $\ln\Sigma$ ” dependences (Figs. 4, 5), the data for different metals, semiconductors and oxides were used [59]. On the one hand, it means that the decreasing of $\Delta\theta$ and T_c with the increasing Σ is a rather general phenomenon. On the other hand, it is clear that the shapes of faceting/roughening diagrams for the same Σ should be different in different materials. Later the numerous works have appeared which permits one to compare the faceting–roughening phase diagrams for the same fcc lattice and the same Σ for metals

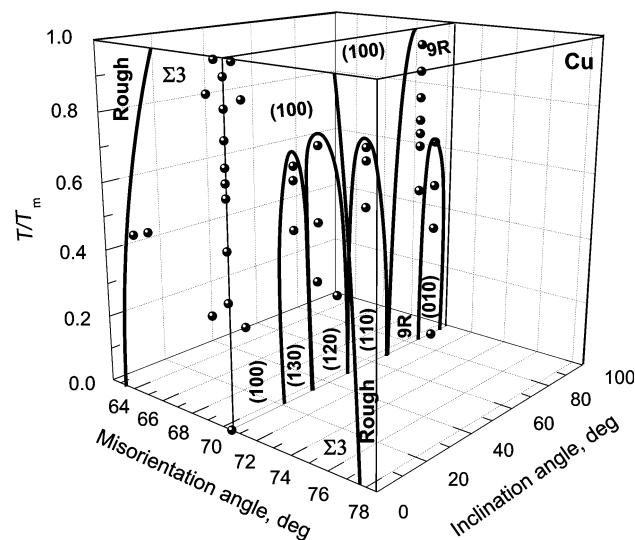


Fig. 9 Three-dimensional phase diagram for the $\Sigma = 3$ twin GBs in Cu in the “Relative temperature T/T_m —misorientation angle θ —inclination angle φ ” coordinates (T being the annealing temperature, T_m being the melting temperature of Cu). Zero value of inclination angle $\varphi = 0$ corresponds to the symmetric twin GB. Reproduced from [84] with permission from Springer

with different SFE. Even the position of energies of tilt GBs in the total energy spectrum of GBs in polycrystals strongly depends on the SFE [84–86]. We will use for the discussion both the SFE and SFE normalized on Gb value (where G is the shear modulus and b is the Burgers vector taken from [87]).

The SFE of silver is even slightly lower than SFE of copper (SFE in Ag is 22 mJ/m^2 [74], while SFE in Cu ranges according to different sources from 30 to 45 mJ/m^2 [88], and the respective normalized SFEs are $2.4\text{--}3.7 \times 10^{-3}$ for copper and 2.4×10^{-3} for silver). ECS of $\Sigma 3$ GBs in silver close to T_m is very similar to that in copper [89]. It also contains only symmetric twin $(100)_{\text{CSL}}$ facet and non-CSL $82^\circ 9R$ facet. They intersect with each other without any sign of intermediate curved (rough) GB portions. Thus, the roughening temperature T_R is higher than the melting temperature T_m for both facets, similar to copper.

The SFE of Al 140 mJ/m^2 [90] is much higher than that of Cu (the respective normalized SFE is 18.8×10^{-3}). In Fig. 10, the 3D phase diagram for the $\Sigma 3$ twin GBs in Al is shown in the “ T/T_m – θ – φ ” coordinates [84]. We did not find in the literature any evidence that the faceting of $\Sigma 3$ twin GBs in Al can be observed above $\Delta\theta = |\theta - \theta_{\Sigma 3}| = 2^\circ$ [91]. In the experiments with Al bicrystals having $\Delta\theta = 3^\circ$, the short portion of the $(100)_{\text{CSL}}$ facet made contact with rough rounded portions of $\Sigma 3$ GB [92, 93]. It means that the angular interval of the existence of special $\Sigma 3$ GB in Al is much narrower than that in Cu. As seen in Fig. 10a, at $\Delta\theta = 0$ the $\Sigma 3$ twin GBs in Al is completely faceted [93, 94]. Close to the melting temperature two facets exist at the $\Sigma 3$ GB: $(100)_{\text{CSL}}$ and $9R$, similar to Cu. However, the $9R$ non-CSL facet disappears with the decreasing temperature already at $0.8 T_m$. The $(010)_{\text{CSL}}$ facet appears instead along with the $(110)_{\text{CSL}}$ facet. Thus, below $0.8 T_m$, only three crystallographically different facets [namely $(100)_{\text{CSL}}$, $(010)_{\text{CSL}}$ and $(110)_{\text{CSL}}$] exist in Al, and not six as in Cu. In Fig. 10b, the “ T/T_m – $\Delta\theta = 3^\circ$ – φ ” section is shown. It is superposed on the “ T/T_m – $\theta = \theta_{\Sigma 3}$ – φ ” section shown in Fig. 10a. It is clearly seen that only one $(100)_{\text{CSL}}$ facet surrounded by the rough rounded GB portion is present in the Al bicrystal with $\Delta\theta = |\theta - \theta_{\Sigma 3}| = 3^\circ$. Therefore, the existence area of the $\Sigma 3$ twin GBs in Al is much narrower than that in Cu. The contact between facets and rough GB portions has a slope discontinuity (i.e. is of first order) like on the surface of Au [70]. The facet and rounded rough GB portions form the first-order facet-to-rough GB ridges. The number of various CSL-facets at low temperatures is also less than in Cu [84].

The SFE of Mo is 410 mJ/m^2 [95] and is much higher than that of Ag, Cu and Al. (The respective normalized SFE for is 11.9×10^{-3} and lies between that of Al and

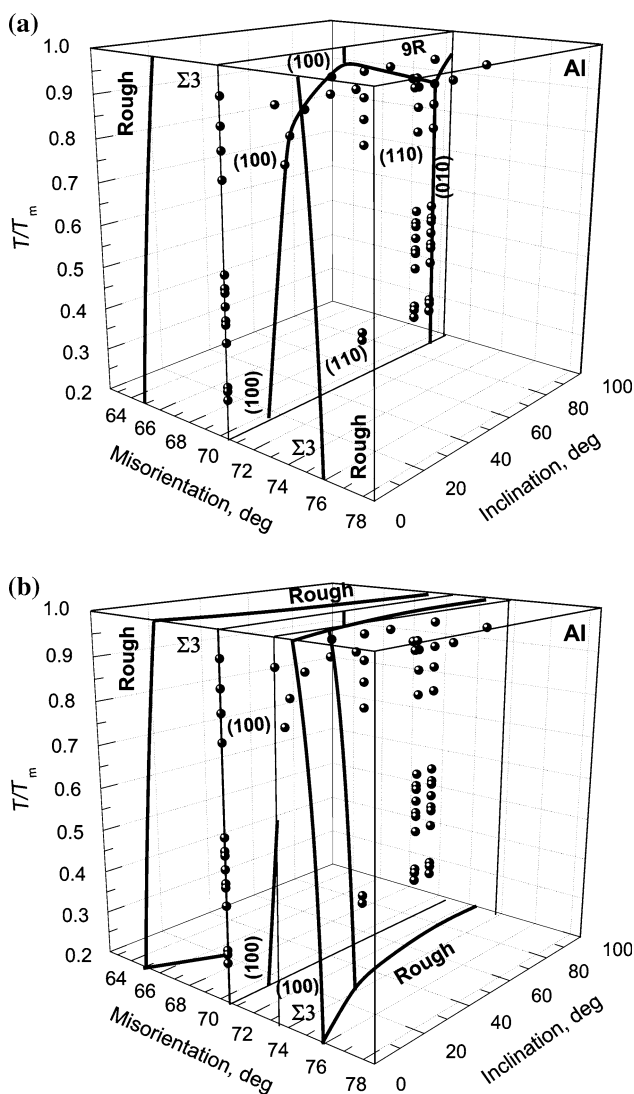


Fig. 10 Three-dimensional phase diagram for the $\Sigma 3$ twin GBs in Al in the “Relative temperature T/T_m —misorientation angle θ —inclination angle φ ” coordinates. **a** $\theta = \theta_{\Sigma 3}$. **b** same as Fig. 10a with additional data for $|\theta - \theta_{\Sigma 3}| = 3^\circ$. Reproduced from [84] with permission from Springer

those for copper and silver.) The energy ratio of the coherent twin boundary and average $\Sigma 3$ GB in Mo is 0.26 [96]. It is close to the similar ratio in Fe (0.25, [62, 97, 98]) and to the energy ratio of the coherent twin boundary and ordinary GBs in Fe–Si alloys (0.22, [97]). These ratios are much higher than those for the fcc metals (for example, the coherent twin energy in fcc Ni is reported as 0.064 J/m², or 0.058 of the average boundary energy [42]). Nevertheless, the coherent twins in Mo, similar to the fcc metals, possess the lowest possible energy among high-angle GBs [44].

In Fig. 11, the 3D phase diagram for the $\Sigma 3$ twin GBs in specially grown [99] Mo bicrystals is shown in the “ $T/T_m - \theta - \varphi$ ” coordinates [84]. We did not find in the literature any evidence that the faceting of $\Sigma 3$ twin GBs in Mo

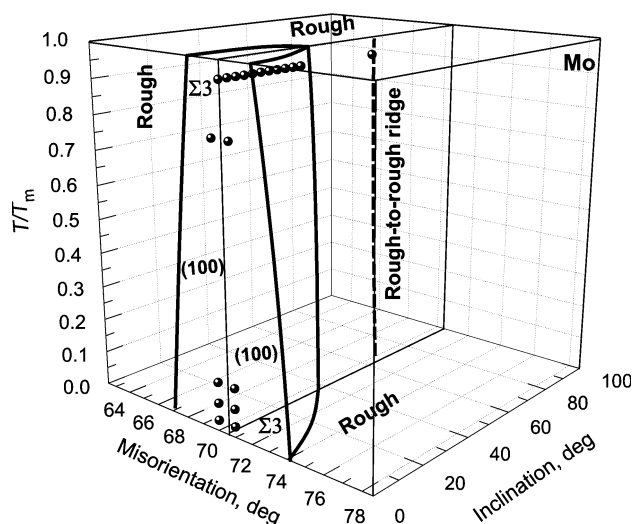


Fig. 11 Three-dimensional phase diagram for the $\Sigma 3$ twin GBs in Mo in the “Relative temperature T/T_m —misorientation angle θ —inclination angle φ ” coordinates. Vertical dotted line at $\theta = \theta_{\Sigma 3}$, $\varphi = 60^\circ$ marks the position of the first-order rough-to-rough ridge. Reproduced from [84] with permission from Springer

can be observed above $\Delta\theta = |\theta - \theta_{\Sigma 3}| = \pm 0.5^\circ$ [100]. The circular $\Sigma 3$ twin GB in a Mo bicrystal contains only two parallel flat facets, namely $(111)_1 \parallel (111)_2$ STGBs or $(100)_{\text{CSL}}$ facets [101]. Both flat $(100)_{\text{CSL}}$ facets contact with rounded rough GB portions. This fact is reflected in Fig. 11. The existence area of $(100)_{\text{CSL}}$ facet is surrounded by the rough GB area. The flat $(100)_{\text{CSL}}$ facets form smooth edges (no slope discontinuity) with rounded rough GB portions. This roughening behaviour is similar to that of facets on the surface of small lead balls [71].

Four slope discontinuities between two rounded rough GB portions were also observed. All of them are in the same crystallographic position and are shown in Fig. 11 by one vertical line at $\varphi = 60^\circ$ [101]. This was the first experimental observation of the first-order rough-to-rough ridges theoretically predicted by the Davidson–den-Nijs model [9, 10]. Similar slope discontinuities were observed in Nb [76]. Therefore, GBs allow one to observe a broad diversity of faceting/roughening phenomena which is quite different and complementary to that of faceting/roughening of free surfaces [102, 103].

The curved $\Sigma 3$ GBs in cubic yttria-stabilized zirconia bicrystals also tend to decompose into two families of facets, namely symmetric $\{111\}/\{111\}$ and asymmetric $\{111\}/\{115\}$ facets. The faceting is preferred in spite of the increasing GB area to about 6 % [104].

The SFE in zinc according to different sources ranges from 160 to 200 mJ/m² [105] and is much higher than that of copper and silver but lower than that of aluminium and molybdenum. The normalized SFE in zinc is $27.8\text{--}34.7 \times 10^{-3}$ and, therefore, higher than all SFEs for Ag,

Cu, Al and Mo. However, crystallographically, the twins in zinc are very different from $\Sigma 3$ twins in Ag, Cu, Al and/or Mo. The c/a value is irrational in Zn (as well as in other metals with hexagonally close-packed lattice), a being the lattice spacing in the basal plane (0001) and c being the lattice spacing in the direction normal to the (0001) plane. Therefore, the exact CSL exists in Zn only for GBs with rotation around [0001] axis. In all other cases, the so-called constrained CSL approach should be used (CCSL) [105–111, 115]. The parallel elongated sides of the twin plate are formed by the coherent symmetric twin $(1\bar{1}0\bar{2})_1 \parallel (1\bar{1}0\bar{2})_2$ grain boundary (STGB) facets [112]. The faceting/roughening behaviour of twin GBs in zinc is quite different in comparison with fcc counterparts. On the one hand, the $(1\bar{1}0\bar{2})_1 \parallel (1\bar{1}0\bar{2})_2$ STGB in Zn remains faceted up to T_m , similar to $(111)_1 \parallel (111)_2$ STGB in Cu, Al and Mo. Moreover, the GB half loop between two parallel symmetric portions of twin GB become completely rounded (rough) at T_R which is very close to T_m . This behaviour is very similar to that of Al. It has to be underlined that the SFE of Zn is also close to that of Al. On the other hand, below the roughening temperature T_R , the faceting of asymmetric twin GBs in zinc (twin tip) differs a lot from that of Cu, Al and Mo. Below 360 °C, the twin tip contains only one plane facet 1 which is nearly parallel to the $(\bar{1}10\bar{2})_2$ plane and has the angle of 84° with the coherent STGB. Above 360 °C, the second facet 2 appears at the tip of the twin plate. This facet is nearly parallel to the $(1\bar{1}00)_1$ plane and has the angle of 46° with the coherent STGB. Between 360 and 410 °C, both 84° and 46° facets coexist, and 84° facet gradually disappears with the increasing temperature. Above 410 °C, only 46° facet is present in the twin tip [112].

Transformation of GB facets into rough-to-rough ridges

The first-order rough-to-rough GB ridge has been observed for the first time in Mo [101]. It has been observed in Zn how two first-order facet-to-rough ridges separated by a GB facet merge together with the increasing temperature and form a first-order rough-to-rough GB ridge (Fig. 12) [113, 114]. This phenomenon was observed in tilt $[10\bar{1}0]$ GB with $\theta = 30^\circ$. At low temperatures, a GB loop has a facet dividing two first-order facet-to-rough ridges (Fig. 12a). This facet is parallel to the closely packed plane of a constrained coincidence sites lattice (CCSL) for the $30^\circ [10\bar{1}0]$ (Fig. 12c, d). It is interesting that the tangents to the rough GB portions in the end-points of the facet are also parallel to closely packed CCSL planes. By increasing the temperature, the facet between points disappears (Fig. 12b, c), and the first-order rough-to-rough GB ridge is

formed instead of two first-order facet-to-rough GB ridges. However, the orientation of the first-order rough-to-rough GB ridge is not arbitrary. The tangents to the rough GB portions in the ridge point remain parallel to the to closely packed CCSL planes (Fig. 12c, d) [113, 114]. The transformation of the facet into the first-order rough-to-rough GB ridge proceeds at $T_{R+} = 400$ °C. The back-transformation of the first-order rough-to-rough GB ridge into is reversible proceeding with a certain hysteresis at $T_{R-} = 395$ °C. The individual first-order rough-to-rough GB ridges also strongly slow down the GB migration in zinc [116].

Faceting–roughening of first and second orders

According to Gibbs and Cahn [1, 2, 117, 118], the surface (or interface) free energy can define the surface (interface) 2D-phases and respective phase transformations. The rough (rounded) portions of surface or interface or crystallographically different facets are such 2D-phases. If the flat (faceted) and rough (rounded) parts of a surface or GB coexist, they meet at edges, which may be either sharp (slope discontinuity) or smooth (no slope discontinuity). In the first case, the faceting/roughening are of first order, whereas in the latter case, it is of second order (continuous). Smooth edges between flat facets and rounded rough regions can belong to the so-called Pokrovsky–Talapov (PT) [122] or Andreev [121] universality class. They have been observed in lead [71] and helium crystals [119, 120]. In most cases, one observes the first-order facet-to-rough ridges in GBs [92, 93, 112]. The second-order (continuous) facet-to-rough ridges have been observed for the first time in tube-like $\Sigma 3$ twin GBs in Mo bicrystals [101]. The circular $\Sigma = 3$ twin GB in a Mo bicrystal contained only two parallel flat facets, namely $(111)_1 \parallel (111)_2$ STGBs or $(100)_{\text{CSL}}$ facets. The flat $(100)_{\text{CSL}}$ facets form smooth edges (no slope discontinuity) with rounded rough GB portions. This roughening behaviour is similar to that of facets on the surface of small lead balls [71]. Near a smooth edge the shape of the curved interface varies as (see Fig. 13):

$$y = A(x-x_c)^\beta + \text{higher order terms} \quad (2)$$

The position of edge is given by x_c . The exponent β is a critical index. The rough GBs curve away from the plane of the $(100)_{\text{CSL}}$ facets as x^β with $\beta = 1.69 \pm 0.07$ on one side and $\beta = 1.72 \pm 0.07$ on the other side of a facet. In similar tubular Nb bicrystals, the values $\beta = 1.61 \pm 0.09$ and $\beta = 1.46 \pm 0.09$ were observed [76].

There are two main models predicting β values. The Andreev mean field approach to the problem of crystal shape neglecting the fluctuations employs a Landau-type expansion of the free energy near the roughening transition

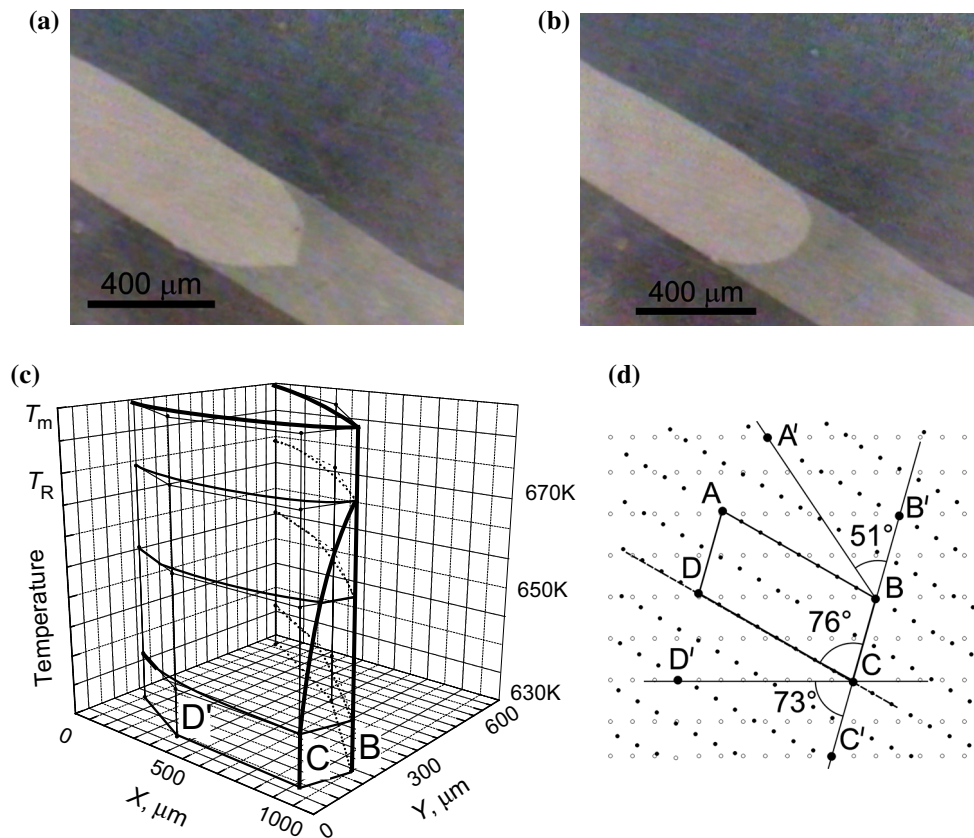


Fig. 12 Optical micrographs of $30^\circ [10\bar{1}0]$ tilt GB: **a** The long facet and two first-order facet-to-rough ridges, $T = 370^\circ\text{C}$, below T_R . **b** The first-order rough-to-rough ridge, $T = 405^\circ\text{C}$, above T_R . The short facet and two first-order facet-to-rough ridges, $T = 400^\circ\text{C}$. **c** Scheme of the temperature influence on the shape of GB loop with a facet between two first-order facet-to-rough ridges at temperatures below T_R and with a first-order rough-to-rough ridge above T_R . Reproduced from [113] with permission from Elsevier. **d** Section of CCSL normal to the $[10\bar{1}0]$ tilt axis for the GB with misorientation angle $\theta = 30^\circ$ in Zn. Filled and empty circles mark the sites of two

misoriented Zn lattices. Large circles mark the sites of the CCSL. The inverse density of coincidence sites is $\Sigma = 15$. Reproduced from [197] with permission from Carl Hanser Verlag. Unit cell of respective CCSL (ABCD), position of basal plane (0001) for grain 2 (CD, dashed line) and position of CCSL plane BC parallel to the facet in the moving GB part are also shown. CCSL planes CD' and BA' are nearly parallel to the tangents to the lower and upper rounded GB portions in their intersection points with a facet (below T_{R-}) or with each other (above T_{R+})

Fig. 13 Scheme for the quantification of a curved GB portions close to the $(100)_{\text{CSL}}$ facet in Mo. Reproduced from [101] with permission from APS



of II order [121]. It delivers $\beta = 2$, which is the signature of the square-law effective interaction between steps. The value $\beta = 2$ has never been observed experimentally. Pokrovsky and Talapov discussed the structure of a monolayer deposited on a periodic substrate incommensurate with the periodicity of the monolayer itself [122]. The steps occurring in the vicinal surface play the role of the boundaries separating individual commensurate regions

in the model [122]. This theory predicts the $\beta = 3/2$. Therefore, we find for the GB roughening the β values which are distinctly below the mean-field prediction and are more consistent with PT theory. In the investigation of ECS of Pb particles, it has been observed that the critical exponent β measured near a (111) facet is not completely universal and varies with azimuthal angle [71]. The β values distinctly fall into two groups: the first mean value is

about 1.7 (similar to our value for Mo twin GB), and the second is almost equal to $3/2$. It has been shown that the β value depends on how the steps interact at the vicinal surface. Scanning tunnelling microscopy demonstrates that these steps can expose either (100) or (111) microfacets [123]. Higher exponents are connected with (100) step ledges. In the case of $\Sigma 3$ GBs, in Mo, the difference between the measured β and theoretical PT values can be due to similar GB steps.

In [124], the faceting of the almost stationary $[10\bar{1}0]$ tilt grain boundary with a misorientation angle θ of 84° in the Zn bicrystal has been investigated. The shape of the very slow migrating grain boundary has been studied in situ between 350 and 400 °C using polarized light. Two intersecting facets lie in the closely packed planes of the CCSL with coincidence parameter $\Sigma = 15$. In the as-grown sample, flat grain boundary facets formed the sharp first-order ridge with the break of the first derivative $\partial y/\partial x$ of the grain boundary shape similar to those observed previously for GB faceting in Zn [109, 113, 114]. However, above 350 °C, the sharp first-order ridge is substituted by the smooth GB portion (Fig. 14) without a $\partial y/\partial x$ derivative break similar to that observed in twin GBs in Mo. The transformation of the as-grown first-order grain boundary ridge into continuous one has been observed for the first time. The critical parameter α has been calculated (Fig. 15) using the grain boundary shape in the transition region. α increases from $\alpha = 1.7 \pm 0.07$ for 350 °C to $\alpha = 1.9 \pm 0.07$ for 385 °C approaching the $\alpha = 2$ value predicted in the mean-field Andreev model for the continuous surface roughening.

Faceting–roughening is the reversible GB phase transition. It was observed initially by in situ heating and cooling in the transmission electron microscope at $\Sigma 11$ GB in Al near the melting temperature T_m [53]. It has been also observed in zinc in situ that the length of the facet gradually decreases with the increasing temperature and becomes zero at the roughening temperature [112, 125]. Upon cooling below the roughening temperature, the facet appears again but with a certain hysteresis of about 5 K [125]. The CSL facets forming first-order ridge with each other or with rough GB portions were observed not only in metals, but also in polysilicon [126, 127], GaN [128], PbTe [129], WC [130] and texturally equilibrated rocks [131].

Influence of impurities on GB faceting–roughening and connection with wetting phenomena

GB wetting and faceting phenomena are intimately connected together [58, 132]. The Bi-induced GB faceting of $\Sigma 3$ GBs in copper has been observed already in the beginning of 1990s [133, 134]. The minor additions of

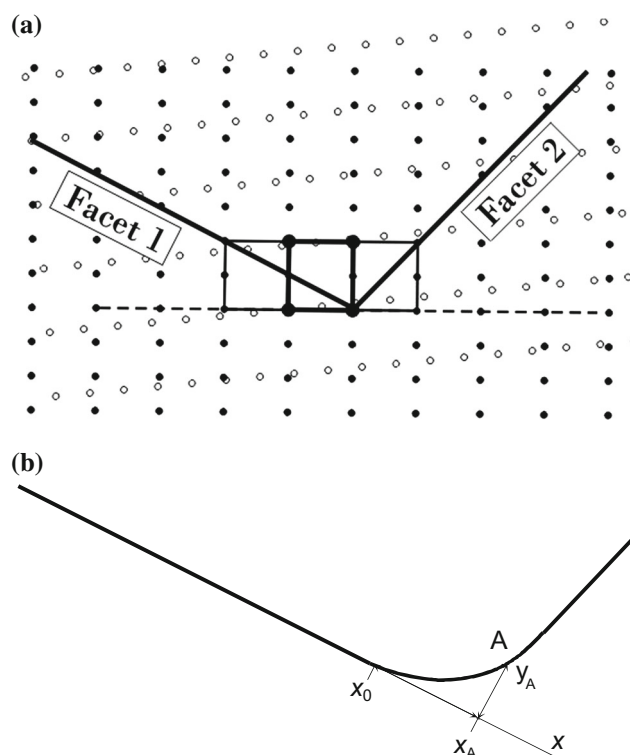


Fig. 14 **a** Section of CCSLs normal to $[10\bar{1}0]$ tilt axis for GBs with misorientation angles θ of 84° . Filled and empty circles mark the sites of two misoriented Zn lattices. Large circles mark the sites of the CCSL. The inverse density of coincidence sites is $\Sigma = 15$. The unit cell of respective CCSL, position of basal plane (0001) for one of the grains and the position of the most closely packed plane in the CCSL are also shown. **b** Scheme for the quantification of a curved GB portion close to the facet is shown. Reproduced from [124] with permission from Carl Hanser Verlag

bismuth, sulphur and tellurium in nickel [135] as well as selenium and tellurium additions in iron [136, 137] also lead to strong GB faceting. In [138], the faceting of $\Sigma 3$ and $\Sigma 9$ tilt GBs has been studied in bicrystals of pure Cu and Cu–Bi alloys containing 2.5×10^{-3} , 10×10^{-3} and 16×10^{-3} at.% Bi close to the melting temperature. The $(100)_{\Sigma 3\text{CSL}}$ and non-CSL $\Sigma 3$ $82^\circ 9R$ facet were observed for $\Sigma 3$ GB. In case of $\Sigma 9$ GB, the $(100)_{\Sigma 9\text{CSL}}$, $(-110)_{\Sigma 9\text{CSL}}$, and $(-120)_{\Sigma 9\text{CSL}}$ facets were observed. The ratio between GB energy, σ_{GB} , and the surface energy, σ_{sur} , was measured by AFM using the GB thermal-groove method. The GB energy and thermal-groove deepening rate increased slightly between 0 and 10×10^{-3} at.% Bi for all facets studied. However, between 10×10^{-3} and 16×10^{-3} at.% Bi, the GB energy increased dramatically [from a factor 2 for the $\Sigma 9(110)$ facet to 15 times larger for the $\Sigma 3(100)$ facet]. The thermal-groove deepening rate also increased by a factor of 10 in this concentration range. This change corresponds well with the GB solidus line (i.e. the formation of a stable layer of a liquid-like GB phase called

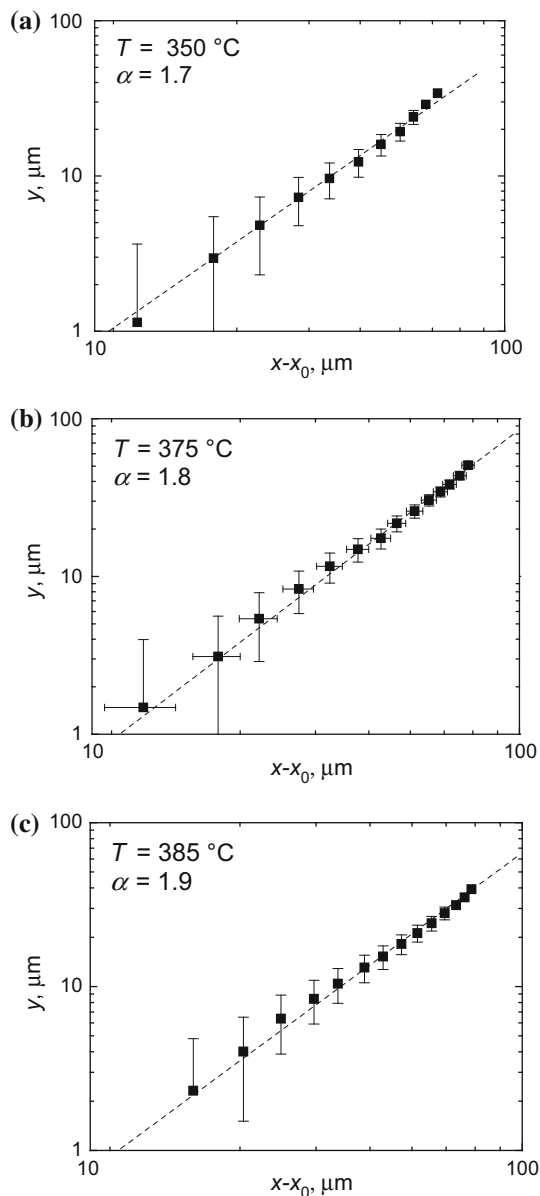


Fig. 15 Shapes of the rounded GB portion at different temperatures in scaling coordinates: **a** 350 °C, **b** 375 °C, **c** 385 °C. Reproduced from [124] with permission from Carl Hanser Verlag

GB prewetting or GB complexion) [76, 78, 139]. Wulff diagrams were constructed using measured σ_{GB}/σ_{sur} values.

The behaviour of $\Sigma 9$ facets is quite complicated with the increasing Bi concentration c . The respective phase diagram for $\Sigma 9$ facets is shown in Fig. 16. Open squares denote the stable facets, and crosses denote the metastable facets. The lines mark the angular areas $\chi(h)$ for the respective ECS facets. With the increasing c , the $(-410)_{\Sigma 9CSL}$ area becomes broader at the cost of $2(100)_{\Sigma 3CSL}$ areas up to 10×10^{-3} at.% Bi. Between 10×10^{-3} and 16×10^{-3} at.% Bi, the $(100)_{\Sigma 3CSL}$ area shrinks, and two new facets $(-410)_{\Sigma 9CSL}$ and $(-230)_{\Sigma 9CSL}$

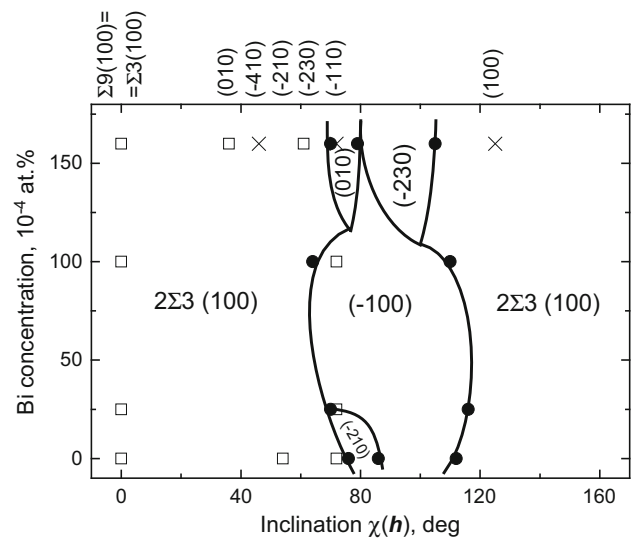


Fig. 16 Bi concentration versus inclination for $\Sigma 9$ tilt GBs in Cu. Reproduced from [138] with permission from Elsevier

appear. The facet $(-120)_{\Sigma 9CSL}$ becomes metastable between 0 and 2.5×10^{-3} at.% Bi. Therefore, the GB prewetting phase transition increases the number of stable $\Sigma 9$ facets between 10×10^{-3} and 16×10^{-3} at.% Bi. This fact explains the early data obtained in the Cu–Bi polycrystals [140, 141]. The numbers of faceted GBs in Cu– 3×10^{-3} at.% Bi [141] and Cu– 9×10^{-3} at.% Bi [140] polycrystalline alloys were low since the Bi content in these alloys is below the GB solidus concentration. However, the number of faceted GBs in Cu– 30×10^{-3} at.% Bi alloys was very high [140] because this concentration is well above the GB solidus. The formation of facets after doping of Cu $\Sigma 11$ bicrystal with bismuth has been directly observed in [142].

Melt- or fluid-filled pore geometry in texturally equilibrated rocks is characterized by various dihedral angles and degrees of faceting. In [143], it was investigated quantitatively by measuring the grain boundary wetness ψ , which is defined as the ratio of solid–liquid boundary area over the total area of interphase boundaries. The wetness ψ increases monotonically with the increasing liquid volume fraction ζ . For systems showing no faceting and low dihedral angle, the relation between ψ and ζ agrees well with the theoretical prediction for an ideal isotropic model assuming tetrakaidecahedral packing. This is true for the olivine–basalt system, whereas partially molten lherzolite shows systematically lower wetness. For systems showing strong faceting, the wetness is systematically lower than the theoretical prediction. The developed faceting model can be used to predict ψ in texturally equilibrated rocks, in particular to calculate the seismic wave velocities of partially molten peridotites [143].

Recently, the aberration-corrected HAADF-STEM permitted to characterize the GBs in 500-ppm Hf-doped polycrystalline alumina [144]. By combining results from experimental images taken at different values of defocus with HAADF image simulation, a novel and general view of the Hf segregation behaviour has emerged. For the outermost cation (GB) layer of one grain, there was extensive substitution of the Al^{3+} ions by Hf^{4+} ions. The Hf-rich layer contained steps/facets both parallel and normal to the beam direction. The step height corresponded to a single atomic layer both normal and parallel to the beam direction [144].

The GBs and their triple junctions (TJs) [145] can be wetted not only by the melt, but also by the second solid phase [146]. In [147], the cold-deformed Cu–Ni–Sn wires were recrystallized by a short-term annealing at 850 °C, close to the solidus of the alloy. Slow cooling of the alloys resulted in faceted GBs. Planar precipitates of $(\text{Cu,Ni})_3\text{Sn}$ were detected at the facets. The high-energy GB facets were covered by the $(\text{Cu,Ni})_3\text{Sn}$ phase (complete GB wetting by a second solid phase), but the low-energy GB facets were free from precipitates [147]. Similar to this phenomenon, the low-energy symmetric twin GBs $(100)_{\Sigma 3\text{CSL}}$ in Cu–Sn alloy were dry, but the high-energy $9R$ facets were wetted and contained the droplets of the liquid phase [148]. One can introduce different dopants in the GBs of artificially prepared bicrystals of yttria-stabilized zirconia (YSZ) [149]. The doping elements and intermediate layers ($\text{Y}_3\text{Fe}_5\text{O}_{12}$ and SrTiO_3) were introduced by depositing thin films on the contact surfaces of YSZ crystals prior to the solid-phase sintering of grains. Depending on the amount and type of deposited material,

the GB continuous intermediate layer (complete wetting by a second solid phase), or nanoscale precipitates (incomplete wetting) at the GB can be obtained. For relatively small misorientation of adjacent grains, the GB faceting and formation of different types of GB dislocations were revealed [149].

Faceting–roughening of low-angle grain boundaries

The low-angle GBs with $\theta < 15^\circ$ – 20° are constructed of the dislocations arrays or networks [150]. The positions of these lattice dislocations are not arbitrary but depend on mutual orientation and misorientation of glide planes. This is the reason why low-angle GBs can also facet, even without CSL. The shape evolution and migration of $\langle 100 \rangle$ and $\langle 111 \rangle$ tilt GBs in Al with rotation angles θ in the range between 6° and 24° were investigated in situ in a scanning electron microscope at elevated temperatures [151–153]. The results revealed that boundaries with misorientation $\theta < 15^\circ$ did not attain a continuously curved shape in the entire temperature range up to the melting point and, thus, did not move under a capillary driving force. Instead, they remained straight or formed several facets which were inclined to the initial boundary orientation. Molecular statics simulations suggested that the observed behaviour of low-angle GBs is due to the anisotropy of grain boundary energy with respect to boundary inclination (Fig. 17). This anisotropy diminishes with the increasing misorientation angle, and high-angle boundaries assume a continuously curved shape and move steadily under the curvature driving force. The faceting of low-angle GB disappears with the increasing temperature T and

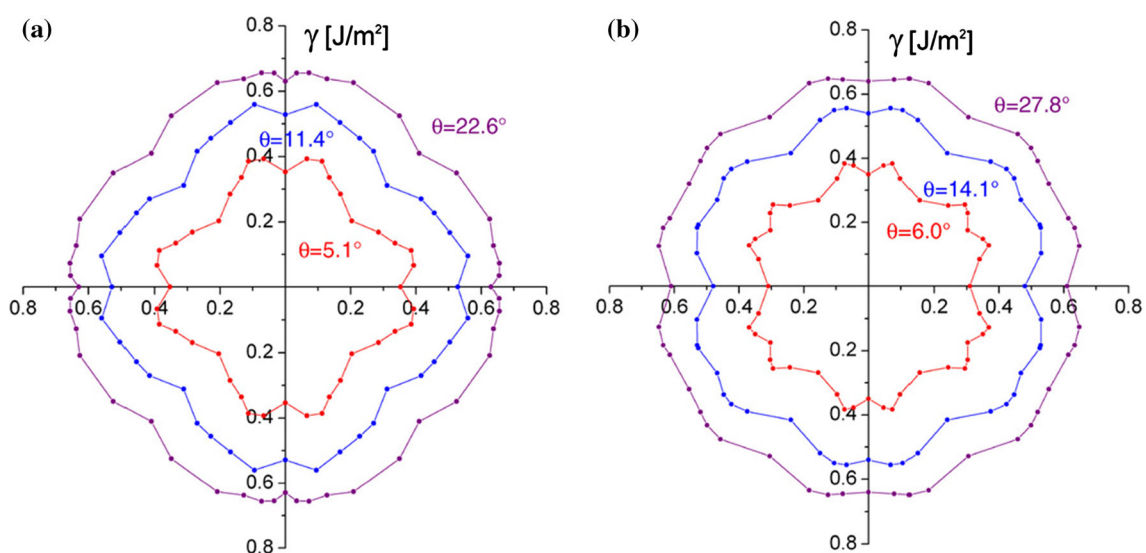


Fig. 17 Computed Wulff plots for **a** 5.1° , 11.4° and 22.6° $\langle 100 \rangle$; and **b** 6.0° , 14.1° and 27.8° $\langle 111 \rangle$ tilt GBs ($T = 0$ K). Reproduced from [151] with permission from Elsevier

misorientation angle θ , and they become rough (continuously curved) [154]. Above a certain misorientation angle θ , the lattice dislocations in the low-angle GBs merge and become indistinguishable, the 2D-row (or array) of 1D-defects transforms into true 2D-defect, and the driving force for low-angle GB faceting disappears. The faceting of low-angle GBs was observed not only in metals [155] but also in Y–Ba–Cu-, Y–Ca–Ba–Cu- and Bi–Sr–Ca–Cu-based oxides [156–158].

The role of grain boundary faceting–roughening in various processes

Abnormal grain growth

Abnormal or discontinuous grain growth, is a grain growth phenomenon through which certain energetically favourable grains grow rapidly in a matrix of finer grains resulting in a bimodal grain size distribution. The computer simulation predicted that the spontaneous transition from the normal to abnormal grain growth takes place if the spread of GB mobilities is high enough [159]. In case of 3D grain growth, the quickest GBs have to move 3.5 times faster than the slowest ones. In case of 2D grain growth (each grain has faces on the top and bottom of a plate or film), the difference between quick and slow GBs is only 2.5 [159]. If the mobility spread is between 2.5 and 3.5, the abnormal grains appear when, during the grain growth, the 3D grain structure becomes 2D [160]. What are the reasons of GB mobility difference?

Most generally accepted model explaining the transition from normal to abnormal grain growth is based on the so-called Zener's model for particle pinning of GBs [161–163]. Pinning of GBs by second-phase particles was modelled by Zener [164] who proposed that particles occupying a grain boundary simply reduce the overall grain boundary energy by a value given by the occluded grain boundary area. This value can be expressed as a pressure which opposes the grain growth pressure. The Ostwald ripening of particles decreases the number of pinning sites. Then, the ability of particles to pin GBs decreases and triggers the quick growth of a few grains at the cost of others. The GBs can be dragged not only by particles (Zener drag) but also by solved atoms (solute drag) or thermal grooves (especially important for thin films) [161].

The rapid migration of certain GBs can be driven by the GB wetting transition like in electrodeposited nanocrystalline Ni and Ni–Fe alloys containing sulphur [165]. The GBs wetted by the layer of a liquid phase become more mobile and allow a growing grain to “run-away” from the fine-grained matrix. Similarly, the low melting temperature of the Nb-rich, Ba-poor phase at the GBs caused localized

liquid-phase sintering, resulting in abnormal grain growth in the strontium barium niobate $\text{Sr}_{0.6}\text{Ba}_{0.4}\text{Nb}_2\text{O}_6$ ceramics or lead zirconate titanate [166, 167]. Accumulation of impurities in GBs also leads to the formation of GB liquid films and to increase of mobility of certain GBs [160, 168–170]. In this review, it is interesting for us to investigate how the GB faceting–roughening influences the transition from normal to abnormal grain growth. Even if this transition is due to the impurity accumulation and formation of layers of GB phase (complexions or liquid films), the GBs frequently possess the large flat facets [165, 167–172]. GB faceting–roughening is the intrinsic driving force for the transition from normal to abnormal grain growth even in the absence of other reason like impurity or Zener drag. If all GBs have a rough structure, then a nearly isotropic normal grain growth occurs. The abnormal grain growth is observed to occur when all or a fraction of the GBs are faceted [126, 160, 173–184]. Below follows the detailed discussion of the works [126, 160, 173–184].

There appear to be two possible mechanisms for linking the faceted grain boundary to abnormal grain growth. The first is the junction stability with singular boundaries, proposed by King [185] and the second is the step growth [186] which becomes continuous at high driving forces [187]. The GB steps are either produced by 2D nucleation or existing at the junctions with dislocations.

The correlation between GB faceting and abnormal grain growth, on the one hand, and GB roughening and normal grain growth, on the other hand, has been observed in many systems. For example, a correlation between grain boundary faceting and abnormal grain growth has been observed in recrystallized polycrystalline Ni at varying annealing temperatures, with or without carbon added [174, 175]. Carburized Ni specimens deformed to 50 pct show faceted GBs and abnormal grain growth when annealed at temperatures below $0.7 T_m$, where T_m is the melting point of Ni in absolute scale. When annealed at or above $0.7 T_m$, the GBs are smoothly curved and, therefore, have a rough structure, and normal grain growth is observed. In silver, the abnormal grain growth occurred during anneals at low temperatures (700, 600 and 500 °C, when a certain portion of GBs was faceted), and at high temperatures (920 and 800 °C when all GBs were rough or non-faceted), the normal grain growth took place [176]. Similar effect of temperature and resulting GB faceting–roughening has been observed in stainless steel [177–179] and in Fe–Si alloys [180]. Thus, when commercial 316L stainless steel specimens are heat treated in a single-phase state at 1100 °C, abnormal grain growth occurs, and some GBs are faceted with hill-and-valley structures in TEM. Some segments of these faceted GBs are expected to be singular. When heat treated at 1300 °C, normal grain growth occurs with all GBs smoothly curved. These GBs

are expected to be atomically rough. At intermediate temperature of 1200 °C, the abnormal grain growth still occurs, but there are no excessive large grains observed as in the case of the specimen heat treated at 1100 °C [177].

Another typical material exhibiting abnormal grain growth during processing is barium titanate, BaTiO₃ [181]. It is used for manufacturing of electronic components such as chip capacitors and positive-temperature-coefficient resistors. Since grain size and distribution considerably affect electrical properties, investigators have been attempted to understand the causes of abnormal grain growth. When BaTiO₃ with 0.1 mol% TiO₂ excess was sintered below the eutectic temperature in air, abnormally large grains formed in the matrix of fine BaTiO₃ grains. A TEM observation revealed that almost all the GBs were faceted. On the other hand, however, when the air-sintered sample with faceted GBs was annealed in H₂, the faceted boundaries became defaceted, and the growth of abnormal grains was suppressed, while the growth of the matrix grains was enhanced, showing normal grain growth behaviour. After reannealing the H₂-annealed samples in air, however, the grain growth behaviour and grain boundary structure were found to recover to those observed in the air-sintered sample. From such observations [182, 183, 188] as well as from TEM studies [184], it is concluded that abnormal growth of BaTiO₃ grains observed is related to grain boundary faceting and that boundary faceting is a necessary condition for abnormal grain growth.

Grain boundary migration, diffusion and fracture

GB faceting strongly influences the GB migration [189–195]. As discussed above, by slow migration, the GB shape is close to the ECS. If GB migrates quickly, the combination of faceted and rough portions can be very far from ECS. We described above the complicated temperature dependence of GB faceting of twin GBs in zinc [112]. Below 360 °C, the twin tip contains only one-plane facet which is nearly parallel to the $(\bar{1}10\bar{2})_2$ plane and has the angle of 84° with the coherent STGB. Above 410 °C, only second facet nearly parallel to the $(1\bar{1}00)_1$ plane and having the angle of 46° with the coherent STGB is present in the twin tip. Between 360 and 410 °C, both 84° and 46° facets coexist, and 84° facet gradually disappear with the increasing temperature. Respectively, the temperature dependence of GB mobility in the Arrhenius coordinates demonstrated the GB migration activation enthalpy of 46.6 kJ/mol below 360 °C and above 410 °C, but different pre-exponential factors (1.1×10^{-11} and 7×10^{-9} m²/s, respectively). Between 360 and 410 °C, the values of the apparent migration activation enthalpy are nonphysically high. They were explained by the model of simultaneous

migration of co-existing grain boundary facets based on the concept of weighted mean curvature [112].

In [196], the impact of faceting on the motion of a tilt grain boundary in Zn was studied. The steady-state motion of GB half-loop was recorded in situ. Above 400 °C, the migrating GB half-loop was continuously curved (rough). Below this temperature, a facet appeared and coexisted with the curved GB forming the first-order facet-to-rough ridge. The length of the facet increased with the decreasing temperature. The temperature dependence of the facet length and the steady-state motions of the GB half-loop with and without facet were investigated. A theory for the motion of a faceted GB was proposed. It allowed to explain the observed phenomena and to extract the mobility and the temperature dependence of a moving facet. In [197], the migrating GB TJ formed by three $[10\bar{1}0]$ tilt GBs with misorientation angles θ of 43°, 37° and 6° has been studied. In certain experimental runs, the facet can form in the $\theta = 37^\circ$ $[10\bar{1}0]$ tilt GB. This facet is parallel to the closely packed plane in the CCSL. The length of this facet decreases with the increasing temperature and becomes zero at 415 °C. The temperature dependence of facet length is better described by mean-field Andreev approximation than by the solid-on-solid model. The step energy estimated in the framework of Bonzel approximation [198] is about 0.1 eV/atom. In other experimental runs, the $\theta = 37^\circ$ $[10\bar{1}0]$ tilt GB did not facet and remains rough in the same temperature interval. This fact allowed us to compare the stationary migrations of the same TJ with faceted and rough GBs. TJ formed by faceted GBs migrates at lower rate of 1–2 orders of magnitude in comparison to that of rough TJ (Fig. 18). The nonphysically high value of the apparent migration activation enthalpy of faceted TJ

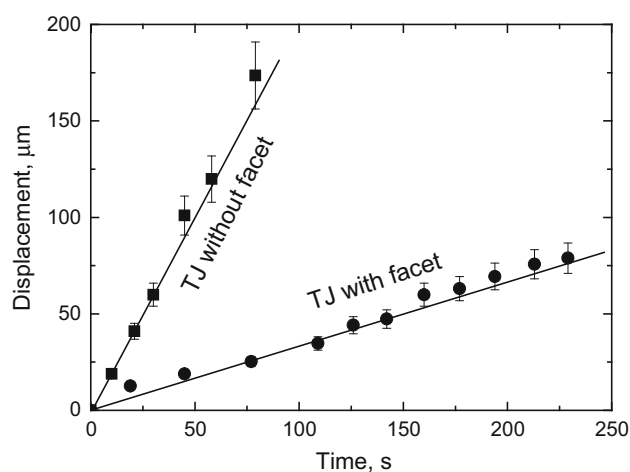


Fig. 18 Time dependence of TJ displacement for TJ with facet and without facet (403 °C). Reproduced from [197] with permission from Carl Hanser Verlag

can appear due to the changing geometry of faceted GB, similar to the case of migration of faceted twin tips.

The GB faceting–roughening influences the GB migration not only in metals but also in ice [199] and oxides [200]. The anisotropy of the GB migration rate in ice was interpreted in terms of the difference in the density of steps among facets: the non-faceted boundary with many steps moves faster than the faceted boundary with fewer steps.

The grain boundary diffusion coefficients along different facets of the same GB can differ more than ten times (like in the case of the gold tracer diffusion along $\Sigma 3$ GBs in copper [201]). GB faceting strongly influences the diffusion-controlled sintering [202]. Namely, a faceted boundary, either fully or partially faceted, is an imperfect atom source for densification [203]. This fact is based on the investigations of effect of GB faceting on densification in a 5 mol% TiO_2 -excess BaTiO_3 . These experimental observations demonstrated the presence of a critical driving force for densification in systems with faceted boundaries and its dependence on boundary faceting, i.e. the critical driving force is larger for systems with greater GB faceting [203].

Intergranular faceting during fatigue is relatively a scarce phenomenon in ductile metals but is known to occur under certain conditions [204]. In the case of bcc steels, it can occur at near-threshold growth rates when the size of the crack tip plastic zone becomes small enough that it is contained within a single grain, and slip is favoured along crystallographic planes. This is known to be due to an effect of moist environments on such steels. Intergranular faceting of bcc steels during fatigue can also occur when hydrogen is dissolved in the crystal lattice. In such cases, depending on the level of dissolved hydrogen and the applied stress, the fracture surface can display a mixed fatigue-fast fracture appearance [205]. Intergranular faceting can also result from grain boundary segregation of phosphorous.

The nature of cyclic plasticity in bcc steels can also lead to intergranular crack initiation and to localization of slip within GBs during subsequent crack growth. The slip-induced intergranular faceting can occur during fatigue of certain ultralow carbon bcc steels. Slip mechanisms in bcc alloys are strongly dependent on temperature, strain rate and interstitial atom content and are governed by the behaviour of long screw dislocations, which are less mobile than non-screw dislocations and make cross-slip more difficult. The core structure of a $1/2$ $[111]$ screw dislocation in a bcc alloy is nonplanar, lying in three $\{111\}$ planes. It spreads into three $1/6$ $[111]$ fractional dislocations which also spread asymmetrically on three $\{112\}$ planes in the twinning sense [206]. This leads to slip asymmetry whereby the shear stress to move a dislocation in one

direction on a slip plane is not the same as that required to move it in the opposite direction on the same plane.

Faceting–roughening in oxides

Faceting–roughening transition takes place also in oxides. Potential GB Wulff shapes for fully faceted GBs at $T = 0$ in alumina were analysed in [58] for a number of various Σ values. Between 1100 and 1600 °C, the $\Sigma 5$ GBs in SrTiO_3 contain various facets parallel to the closely packed planes in CSL [207, 208]. Their number decreases with the increasing temperature, and above 1600 °C, all facets completely disappear [207, 209]. A combination of the impedance spectroscopy, high-resolution transmission electron microscopy (HRTEM), and electron energy loss spectroscopy (EELS) of a 36.8° $[001]$ tilt $\Sigma 5$ grain boundary demonstrated that the changes in GB impedance, GB electronic structure, and the GB faceting–defaceting transition were closely related to each other. The rough grain boundary observed at 1600 °C contained more oxygen vacancies than the faceted GBs observed below 1600 °C. Disordering of grain boundary by the defaceting (roughening) transition appears to have caused the abrupt appearance of GB impedance at 1600 °C [210].

The near $\Sigma 5$ (210)/ $[100]$ GBs in $\text{Y}_3\text{Al}_5\text{O}_{12}$ (YAG) bicrystals after annealing between 400 and 1600 °C contain microfacets in the perfect $\Sigma 5$ zones between intrinsic GB dislocations compensating the mismatch to the exact $\Sigma 5$ misorientation [211]. Strong faceting of tilt GBs was observed in the $\text{YBa}_2\text{Cu}_3\text{O}_{7-x}$ thin films deposited on SrTiO_3 bicrystal substrates [212]. The microfacets and the array of lattice and GB dislocations were observed also in GBs with low $\theta = 8^\circ$ and high $\theta = 41^\circ$ misorientation angles in NiO [213].

GB faceting–roughening in superconductive cuprates with high critical temperature

GBs are usually detrimental for the electrical properties of ceramic superconductors, especially in superconducting cuprates. This can be deduced from the comparison of the critical currents obtained for single crystals and for polycrystalline ceramics [214]. The data measured on thin film bicrystals epitaxially grown on SrTiO_3 bicrystals show that the critical current J_c exponentially diminishes with the increasing misorientation angle θ between adjacent grains [215–219]. At $\theta > 20^\circ$, the critical current reaches a plateau, there are also some indications of cusps in the J_c (θ) dependence which correspond to CSLs [215, 216, 220–223]. This behaviour can be explained by describing the boundary in terms of primary dislocations with a spacing $d = b/2 \sin \theta/2$ (Reed equation for small-angle

GBs [150]). When θ exceeds 20° , d matches the size of the dislocation core [224]. This core can be amorphous or can correspond to a strong perturbation in the atomic structure [224]. Below $\theta = 20^\circ$, the GB contains the segments of perfect contact of abutting grains forming the high- T_c “pathways” crossing the boundary plane. They are separated by dislocation cores with low T_c [219, 225–229]. One can say to a first approximation, that thereafter a continuous insulating layer of 2–3 nm will lead to a constant attenuation of the supercurrent. However, the description of high-angle ($\theta > 15^\circ$) GBs in terms of primary dislocations is not valid. The structure of such boundaries is better approached with the coincidence model [29]. Therefore, according to this description, maxima in the critical current should be observed for specific orientations corresponding to coincidence relationships between the grains. Due to the very small coherence length of ceramics ($3 < \xi < 15 \text{ \AA}$), the behaviour of the boundary is highly dependent on its local structure [230] at the nanometre scale, and even at the angstrom scale. It is not sufficient to know the misorientation between the grains to understand the electrical behaviour of the boundary. One must also gain a precise insight into the interfacial atomic structure. Several papers have been devoted to the imaging of GBs in $\text{YBa}_2\text{Cu}_3\text{O}_{7-x}$ either as a ceramic [231–236] or as a thin film [107, 237, 238] by TEM. These give, in particular, precise information concerning GB segregation and local stress.

TEM studies have revealed that GBs in superconducting cuprates are composed of facets having various orientations and typical dimensions of the order of 10–100 nm [216]. The GB faceting can partially account for the experimentally observed reduction of the critical current density J_c with the increasing grain boundary angle θ . The angular dependence of J_c for individual GB facets may deviate considerably from the $J_c(a)$ dependence observed in standard measurements that employ macroscopic GBs [216]. The faceting leads to an inhomogeneous current distribution in the grain boundary, which is different for the superconducting and the normal states [216]. It is concluded that a necessary condition for GBs to yield a sufficient critical current is a faceted and low-energy configuration as well as orientation relationships, between abutting grains, compatible with the easy propagation of Cooper pairs in Cu–O planes [220, 239]. The interfacial atomic structure which includes atoms common to both crystals should be conducive to a limited decrease in the order parameter. However, the presence of pseudo-periodic microfacets, with a size comparable to the vortex core, should induce an efficient pinning of the magnetic flux [223, 227, 228, 239–243]. From these structural data, and in agreement with measurements on specific coincidence boundaries, it is inferred that the critical current in cuprate ceramics is likely to be increased, if one could markedly

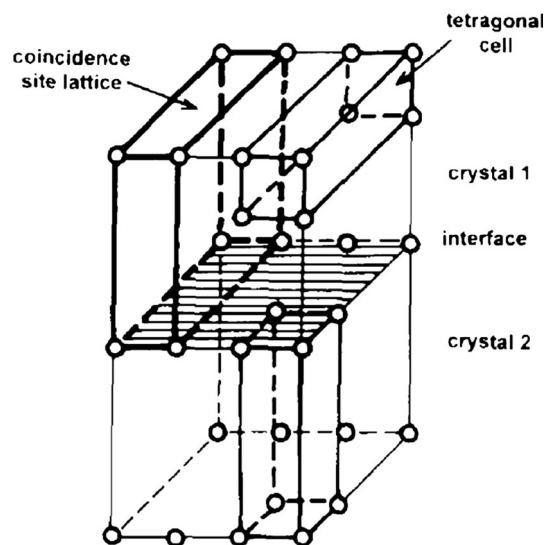


Fig. 19 Scheme of the Σ_3 boundary in cuprates containing the (a, b) plane. It shows the GB, the orientation relationships between crystals 1 and 2, and the coincidence site lattice. Reproduced from [220] with permission from Elsevier

enhance the ratio of coincidence boundaries which do not contain the (a, b) plane (Fig. 19) [220]. Therefore, it would be worth trying to optimize the sintering conditions towards this goal.

Summary and conclusions

GBs in metals, semiconductors and dielectrics can be either flat (faceted) or curved (rough). The facets on free surfaces are parallel to the most densely packed crystal planes. GB are parallel to the most densely packed planes of CSL formed by two lattices of abutting grains. Few non-CSL facets were also observed. Facets exist in restricted areas of misorientation and inclination angles. They gradually disappear with the increasing temperature (faceting–roughening transition). Facets form ridges with rough GB portions. These ridges can be of first order (with shape discontinuity, two tangents in the intersection point) or of second order (continuous transition between flat and curved GBs, common tangent in the intersection point). For the same CSL, faceting is more pronounced for materials with lower SFE. GB facets control the transition from normal to abnormal grain growth and strongly influence the GB migration, diffusion, wetting, fracture and electrical conductivity.

Acknowledgements The authors thank the Russian Foundation for Basic Research (Contracts 14-03-31510 and 14-08-00972), the Russian Federal Ministry for Education and Science (Grants 14.A12.31.0001 and Increase Competitiveness Program of NUST «MISiS» K2-2014-013) and the Polish National Science Centre (Grant OPUS UMO-2014/13/B/ST8/04247) for the financial support.

Compliance with ethical standards

Conflict of Interest The authors declare that they have no conflict of interest.

References

- Gibbs JW (1878) On the equilibrium of heterogeneous substances. *Trans Conn Acad* 3:343
- Gibbs JW (1928) On the equilibrium of heterogeneous substances, vol 3. Longmans, Green & Co., New York
- Curie P (1885) Sur la formation des cristaux et sur les constants capillaire des leur faces differentes. *Bull Soc Min France* 8:145
- Wulff GV (1895, 1896) About rates of growth and dissolution of crystals. *Izvestia Warsaw Univ No. 7–9 and 1,2:1* (in Russian)
- Wulff G (1901) Zur Frage der Geschwindigkeit des Wachstums und der Auflösung von Krystallflächen. *Z Kristallogr* 34:449
- Herring C (1952) The use of classical macroscopic concepts in surface energy problems. In: Gomer R, Smith CS (eds) *Structure and properties of solid surfaces*. University of Chicago Press, Chicago, p 5
- Landau LD, Lifshitz EM (1958) *Statistical physics*, vol V. Addison-Wesley, Reading
- Bonzel HP (2003) 3D equilibrium crystal shapes in the new light of STM and AFM. *Phys Rep* 385:1
- Davidson D, den Nijs M (1999) Temperature dependence of facet ridges in crystal surfaces. *Phys Rev E* 59:5029
- Davidson D, den Nijs M (2000) Facet ridge end points in crystal shapes. *Phys Rev Lett* 84:326
- Taylor JE, Cahn JW, Handwerker CA (1992) Geometric models of crystal growth. *Acta Metall Mater* 40:1443
- Cahn JW, Carter WC (1996) Crystal shapes and phase equilibria: a common mathematical basis. *Metall Mater Trans A* 27:1431
- Curiotto S, Chien H, Meltzman H, Labat S, Wynblatt P, Rohrer GS, Kaplan WD, Chatain D (2013) Copper crystals on the (1,1,-2,0) sapphire plane: orientation relationships, triple line ridges and interface shape equilibrium. *J Mater Sci* 48:3013. doi:10.1007/s10853-012-7080-0
- Klinger L, Rabkin E (2001) Effects of surface anisotropy on grain boundary grooving. *Interface Sci* 9:55
- Saylor DM, Rohrer GS (2001) Evaluating anisotropic surface energies using the capillarity vector reconstruction method. *Interface Sci* 9:35
- Kossel W (1927) Zur Theorie des Kristallwachstums. *Nachr Ges Wissensch Göttingen* 1:135
- Stranski IN (1928) Zur Theorie des Kristallwachstums. *Z Phys Chem* 136:259
- Burton WK, Cabrera N, Frank FC (1951) The growth of crystals and the equilibrium structure of their surfaces. *Trans Roy Soc London A* 243:299
- Gruber EF, Mullins WW (1967) On the theory of anisotropy of crystalline surface tension. *J Phys Chem Solids* 28:875
- Jayaprakash C, Saam WF (1984) Thermal evolution of crystal shapes—the fcc crystal. *Phys Rev B* 30:3916
- Rottman C, Wortis M, Heyraud JC, Métois JJ (1984) Equilibrium shapes of small lead crystals—observation of Pokrovsky-Talapov critical behaviour. *Phys Rev Lett* 52:1009
- Rottman C, Wortis M (1984) Equilibrium shapes for lattice models with nearest-neighbor and next-nearest-neighbor interactions. *Phys Rev B* 29:328
- Holzer M, Wortis M (1989) Low-temperature expansions for the step free energy and facet shape of the simple cubic Ising model. *Phys Rev B* 40:11044
- Fisher DS, Weeks JD (1983) Shape of crystals at low temperatures—absence of quantum roughening. *Phys Rev Lett* 50:1077
- Nozieres P, Gallet F (1987) The roughening transition of crystal surfaces. I. Static and dynamic renormalization theory, crystal shape and facet growth. *J Phys (Paris)* 48:353
- Berezinskii VL (1971) Destruction of long-range order in one-dimensional and two-dimensional systems having a continuous symmetry group. I. Classical systems. *Sov Phys JETP* 32:493
- Berezinskii VL (1972) Destruction of long-range order in one-dimensional and two-dimensional systems having a continuous symmetry group. I. Quantum systems. *Sov Phys JETP* 34:610
- Kosterlitz JM, Thouless DJ (1973) Ordering, metastability and phase transitions in two-dimensional systems. *J Phys C* 6:1181
- Grimmer H, Bollmann W, Warrington DT (1974) Disorientations and coincidence rotations for cubic lattices. *Acta Cryst A* 30:197
- Brandon DG (1966) The structure of high-angle grain boundaries. *Acta Metall* 14:1479
- Hirth JP, Balluffi RW (1973) On grain boundary dislocations and ledges. *Acta Metall* 21:929
- Kronberg ML, Wilson FH (1949) Secondary recrystallization in copper. *Trans AIME* 185:501
- Wagner WR, Tan TY, Balluffi RW (1974) Faceting of high-angle grain boundaries in the coincidence lattice. *Philos Mag* 29:895
- Tan TY, Sass SL, Balluffi RW (1975) The detection of the periodic structure of high angle twist boundaries. II. High resolution electron microscopy study. *Philos Mag* 31:575
- Bollmann W (1970) *Crystal defects and crystalline interfaces*. Springer, New York
- Brandon DG, Ralph B, Ranganathan S, Wald MS (1964) A field ion microscope study of atomic configuration at grain boundaries. *Acta Metall* 12:813
- Wolf D (1985) On the relationship between symmetrical tilt, twist, “special”, and “favoured” grain boundaries. *J Phys Paris* 46:C4–C197
- Fecht HJ, Gleiter H (1985) A lock-in model for the atomic structure of interphase boundaries between metals and ionic crystals. *Acta Metall* 33:557
- Sutton AP, Balluffi RW (1987) On geometric criteria for low interfacial energy. *Acta Metall* 35:2177
- Goodhew PJ, Tan TY, Balluffi RW (1978) Low energy planes for tilt boundaries in gold. *Acta Metall* 26:557
- Chaudhari P, Matthews JW (1971) Coincidence twist boundaries between crystalline smoke particles. *J Appl Phys* 42:3063
- Olmsted DL, Foiles SM, Holm EA (2009) Survey of computed grain boundary properties in face-centered cubic metals: I. Grain boundary energy. *Acta Mater* 57:3694
- Rohrer GS (2011) Grain boundary energy anisotropy: a review. *J Mater Sci* 46:5881. doi:10.1007/s10853-011-5677-3
- Ratanaphan S, Olmsted DL, Bulatov VV, Holm EA, Rollett AD, Rohrer GS (2015) Grain boundary energies in body-centered cubic metals. *Acta Mater* 88:346
- Vitek V, Sutton AP, Smith DA, Pond RC (1980) The dislocation structure of high angle grain boundaries. In: Balluffi RW (ed) *Grain boundary structure and kinetics*. American Society for Metals, Metals Park, pp 115–148
- Ernst F, Finnis MW, Koch A, Schmidt C, Straumal B, Gust W (1996) Structure and energy of twin boundaries in copper. *Z Metallk* 87:911
- Wolf U, Ernst F, Muschik T, Finnis MW, Fischmeister HF (1992) The influence of grain boundary inclination on the structure and energy of $\Sigma 3$ grain boundaries in copper. *Philos Mag A* 66:991
- Ernst F, Finnis MW, Hoffmann D, Muschik T, Schönberger U, Wolf U (1992) Theoretical prediction and direct observation of the 9R structure in Ag. *Phys Rev Lett* 69:620

49. Hofmann D, Finnis MW (1994) Theoretical and experimental analysis of near $\Sigma 3$ (211) boundaries in silver. *Acta Metall Mater* 42:3555
50. Maksimova EL, Shvindlerman LS, Straumal BB (1988) Transformation of $\Sigma 17$ special tilt boundaries to general boundaries in tin. *Acta Metall* 36:1573
51. Straumal BB, Shvindlerman LS (1985) Regions of existence of special and non-special grain boundaries. *Acta Metall* 33:1735
52. Aleshin AN, Prokofjev SI, Shvindlerman LS (1985) Evidence of structure transformation in $\Sigma = 5$ near coincidence grain boundaries. *Scr Metall* 19:1135
53. Hsieh TE, Balluffi RW (1989) Observations of roughening/defaceting phase transitions in grain boundaries. *Acta Metall* 37:2133
54. Kim MJ, Cho YK, Yoon DY (2004) Facet-defacet transition of grain boundaries in alumina. *J Am Ceram Soc* 87:455
55. Rottman C, Wortis M (1981) Exact equilibrium crystal shapes at non-zero temperatures in 2 dimensions. *Phys Rev B* 24:6274
56. Bonzel HP (2001) Surface morphologies: transient and equilibrium shapes. *Interface Sci* 9:21
57. Keshishev KO, Parshin AY, Babkin AV (1981) Crystallization waves in He⁴. *Sov Phys JETP* 53:362
58. Blendell JE, Carter WC, Handwerker CA (1999) Faceting and wetting transition of anisotropic interfaces and grain boundaries. *J Am Ceram Soc* 82:1889
59. Schuh CA, Kumar M, King E (2005) Universal features of grain boundary networks in FCC materials. *J Mater Sci* 40:847. doi:10.1007/s10853-005-6500-9
60. Jin Y, Lin B, Rollett AD, Rohrer GS, Bernacki M, Bozzolo N (2015) Thermo-mechanical factors influencing annealing twin development in nickel during recrystallization. *J Mater Sci* 50:5191. doi:10.1007/s10853-015-9067-0
61. Randle V, Rohrer GS, Miller HM, Coleman M, Owen GT (2008) Five-parameter grain boundary distribution of commercially grain boundary engineered nickel and copper. *Acta Mater* 56:2363
62. Beladi H, Rohrer GS (2013) The relative grain boundary area and energy distributions in a ferritic steel determined from three-dimensional electron backscatter diffraction maps. *Acta Mater* 61:1404
63. Beladi H, Rohrer G (2013) The distribution of grain boundary planes in interstitial free steel. *Metall Mater Trans A* 44:115
64. Glowinski K, Morawiec A (2014) Twist, tilt, and symmetric grain boundaries in hexagonal materials. *J Mater Sci* 49:3936. doi:10.1007/s10853-013-7958-5
65. Ratanaphan S, Yoon Y, Rohrer GS (2014) The five parameter grain boundary character distribution of polycrystalline silicon. *J Mater Sci* 49:4938. doi:10.1007/s10853-014-8195-2
66. Straumal BB, Polyakov SA, Bischoff E, Gust W, Mittemeijer EJ (2001) Faceting of $\Sigma 3$ and $\Sigma 9$ grain boundaries in copper. *Interface Sci* 9:287
67. Straumal BB, Polyakov SA, Mittemeijer EJ (2006) Temperature influence on the faceting of $\Sigma 3$ and $\Sigma 9$ grain boundaries in Cu. *Acta Mater* 54:167
68. Brown JA, Mishin Y (2007) Dissociation and faceting of asymmetrical tilt grain boundaries: molecular dynamics simulations of copper. *Phys Rev B* 13:134118
69. Heyraud JC, Metois JJ (1980) Equilibrium shape of gold crystallites on a graphite cleavage surface—surface energies and interfacial energy. *Acta Metall* 28:1789
70. Heyraud JC, Metois JJ (1980) Establishment of the equilibrium shape of metal crystallites on a foreign substrate—gold on graphite. *J Cryst Growth* 50:571
71. Heyraud JC, Metois JJ (1983) Equilibrium shape and temperature—lead on graphite. *Surf Sci* 128:334
72. Rybin VV, Perevesentsev VN (1975) General theory of grain boundary shifts. *Sov Phys Solid State* 17:2103
73. Gallagher PCJ (1970) The influence of alloying, temperature, and related effects on the stacking fault energy. *Metall Trans* 1:2429
74. Murr E (1975) *Interfacial phenomena in metals and alloys*. Addison Wesley, Boston
75. YaV Kucherinenko, Protasova SG, Straumal BB (2005) Faceting of $\Sigma 3$ grain boundaries in Cu: three-dimensional Wulff diagrams. *Defect Diffus Forum* 237:584
76. Straumal BB, Semenov VN, Khruzhcheva AS, Watanabe T (2005) Faceting of the $\Sigma 3$ coincidence tilt boundary in Nb. *J Mater Sci* 40:871. doi:10.1007/s10853-005-6503-6
77. Lojkowski W, Sodervall U, Mayer S (1998) The effect of pressure on indium diffusion along $\langle 001 \rangle$ tilt grain boundaries in copper bicrystals. *Interface Sci* 6:187
78. Chang L-S, Rabkin E, Straumal BB, Hoffmann S, Baretzky B, Gust W (1998) Grain boundary segregation in the Cu–Bi system. *Diffus Forum* 156:135
79. Straumal BB, Polyakov SA, Bischoff E, Mittemeijer E, Gust W (2003) Grain boundary faceting phase transition and thermal grooving in Cu. *Defect Diffuse Forum* 216:93
80. Straumal BB, Polyakov SA, Chang L-S, Mittemeijer EJ (2007) The effect of bismuth segregation on the faceting of $\Sigma 3$ and $\Sigma 9$ coincidence boundaries in copper bicrystals. *Int J Mater Res (Zt Metallkd)* 98:451
81. Goukon N, Yamada T, Kajihara M (2000) Boundary energies of Sigma 11 [110] asymmetric tilt boundaries in Cu determined from the shape of boundary silica particles. *Acta Mater* 48:2837
82. Gokon N, Kajihara A (2008) Fracture behavior of Sigma 9 [110] asymmetric tilt boundaries in Cu doped with Bi. *Mater Sci Eng A* 477:121
83. Kuhn H, Bärö G, Gleiter H (1979) Energy-misorientation relationship of grain-boundaries. *Acta Metall* 27:959
84. Straumal BB, Baretzky B, Kogtenkova OA, Gornakova AS, Sursaeva VG (2012) Faceting-roughening of twin grain boundaries. *J Mater Sci* 47:1641. doi:10.1007/s10853-011-5807-y
85. Straumal BB, Protsenko PV, Straumal AB, Rodin AO, Kucheev YuO, Gusak AM, Murashov VA (2012) Contribution of tilt boundaries to the total energy spectrum of grain boundaries in polycrystals. *JETP Lett* 96:582
86. Gornakova AS, Straumal BB, Tsurekawa S, Chang L-S, Nekrasov AN (2009) Grain boundary wetting phase transformations in the Zn–Sn and Zn–In systems. *Rev Adv Mater Sci* 21:18
87. Haynes WM (2015) *Handbook of chemistry and physics*, 86th edn. CRC press (Taylor & Francis Group), Boca Raton
88. Carter CB, Ray ILF (1977) On the stacking-fault energies of copper alloys. *Philos Mag* 35:189
89. Barg AI, Rabkin E, Gust W (1995) Faceting transformation and energy of a $\Sigma 3$ grain boundary in silver. *Acta Metall Mater* 43:4067
90. Cai J, Wang F, Lu C, Wang YY (2004) Structure and stacking-fault energy in metals Al, Pd, Pt, Ir, and Rh. *Phys Rev B* 69:224104
91. Dingley DJ, Pond RC (1979) On the interaction of crystal dislocations with grain boundaries. *Acta Metall* 27:667
92. Kogtenkova O, Straumal B, Protasova S, Tsurekawa S, Watanabe T (2005) The influence of misorientation deviation on the faceting of $\Sigma 3$ grain boundaries in aluminium. *Zt Metallkd* 96:216
93. Protasova SG, Kogtenkova OA, Straumal BB (2007) Faceting of individual $\Sigma 3$ grain boundaries in Al. *Mater Sci Forum* 558:949
94. Kogtenkova OA, Straumal BB, Protasova SG, Zięba P (2005) The temperature influence on the faceting of $\Sigma 3$ grain boundaries in aluminium. *Defect Diffus Forum* 237:603

95. Pegel B (1968) Stacking faults on 110 planes in the bcc lattice. *Phys Status Solidi* 28:603
96. Tsurekawa S, Tanaka T, Yoshinaga H (1994) Grain-boundary structure, energy and strength in molybdenum. *Mater Sci Eng A* 176:341
97. Dunn CG, Daniels FW, Bolton MJ (1950) Measurement of relative interface energies in twin related crystals. *J Met* 2:368
98. Dunn CG, Lionetti F (1949) The effect of orientation difference on grain boundary energies. *Trans AIMME* 185:125
99. Semenov VN, Straumal BB, Glebovsky VG, Gust W (1995) Preparation of Fe-Si single crystals and bicrystal for diffusion experiments by the electron-beam floating zone technique. *J Cryst Growth* 151:180
100. Rybin VV, Titovets YuF, Teplitsky DM, Zolotarevsky NYu (1982) Statistics of grain misorientations in molybdenum. *Fiz Metall Metalloved* 53:544 (in Russian)
101. Straumal BB, Semenov VN, Kogtenkova OA, Watanabe T (2004) Pokrovsky-Talapov critical behavior and rough-to-rough ridges of the $\Sigma 3$ coincidence tilt boundary in Mo. *Phys Rev Lett* 92:196101
102. Wynblatt P, Chatain D (2009) Surface segregation anisotropy and equilibrium shape of alloy crystals. *Rev Adv Mater Sci* 21:44
103. Chatain D, Ghetta V, Wynblatt P (2004) Equilibrium shape of copper crystals grown on sapphire. *Interface Sci* 12:7
104. Shibata N, Yamamoto T, Ikuhara Y, Sakuma T (2001) Structure of [110] tilt grain boundaries in zirconia bicrystals. *J Electron Microsc* 50:429
105. Shin K, King AH (1991) Observation of grain boundary structure in zinc. *Philos Mag A* 63:1023
106. Chen F-R, King AH (1987) The further geometry of grain boundaries in hexagonal close-packed metals. *Acta Crystallogr B* 43:416
107. Tietz LA, Carter CB (1991) Special grain boundaries in $\text{YBa}_2\text{Cu}_3\text{O}_{7-x}$ thin films. *Phys C* 182:241
108. Barrett CD, El Kadiri H (2014) The roles of grain boundary dislocations and disclinations in the nucleation of {1,0,-1,2} twinning. *Acta Mater* 63:1
109. Bishop GH, Hartt WH, Bruggeman G (1971) Grain boundary faceting of (1,0,-1,0) tilt boundaries in zinc. *Acta Metall* 19:37
110. Hartt WH, Bishop GH, Bruggeman G (1974) Grain boundary faceting of (1,0,-1,0) tilt boundaries in zinc. 2. *Acta Metall* 23:971
111. Hartt WH, Bishop GH, Bruggeman G (1968) Grain boundary faceting of [1010] tilt boundaries in zinc. *J Met* 20:A71
112. Straumal BB, Rabkin E, Sursaeva VG, Gornakova AS (2005) Faceting and migration of twin grain boundaries in zinc. *Zt Metallkd* 96:161
113. Straumal B, Sursaeva V, Baretzky B (2010) Grain boundary ridges and triple lines. *Scr Mater* 62:924
114. Straumal BB, Gornakova AS, Sursaeva VG (2008) Reversible transformation of a grain boundary facet into a rough-to-rough ridge in Zn. *Philos Mag Lett* 88:27
115. Bruggeman GA, Bishop GH, Hartt WH (1972) Coincidence and near-coincidence grain boundaries in hcp metals. In: Hu H (ed) *The nature and behaviour of grain boundaries*. Plenum, New York, pp 63–122
116. Sursaeva V, Gornakova A, Muktepavela F (2014) Grain boundary ridges slow down grain boundary motion: in-situ observation. *Mater Lett* 124:24
117. Hoffman DW, Cahn JW (1972) A vector thermodynamics for anisotropic surfaces. I. Fundamentals and applications to plane surface junctions. *Surf Sci* 31:368
118. Cahn JW, Hoffman DW (1974) A vector thermodynamics for anisotropic surfaces: II. Curved and faceted surfaces. *Acta Metall* 22:1205
119. Wolf PE, Balibar S, Gallet F (1983) Experimental observation of a 3rd roughening transition on hcp He^4 crystals. *Phys Rev Lett* 51:1366
120. Wagner R, Steel SC, Andreeva OA, Jochemsen R, Frossati G (1996) First observation of (100) and (211) facets on He-3 crystals. *Phys Rev Lett* 76:263
121. Andreev AF (1981) Faceting phase transition of crystals. *Sov Phys JETP* 53:1063
122. Pokrovsky VL, Talapov AL (1979) Ground state, spectrum, and phase diagram of two-dimensional incommensurate crystals. *Phys Rev Lett* 42:65
123. Arenhold K, Surnev S, Coenen P, Bonzel HP, Wynblatt P (1998) Scanning tunneling microscopy of equilibrium crystal shape of Pb particles: test of universality. *Surf Sci* 417:L1160
124. Straumal BB, Gornakova AS, Sursaeva VG, Yashnikov VP (2009) Second-order faceting-roughening of the tilt grain boundary in zinc. *Int J Mater Res (Zt Metallkd)* 100:525
125. Straumal BB, Gornakova AS, Sursaeva VG (2009) Grain boundary faceting-roughening in Zn. *Crystallogr Rep* 54:1070
126. Nakhodkin N, Kulish N, Rodionova T (2010) Faceting of twin grain boundaries in polysilicon films. *Phys Status Solidi A* 207:316
127. Nakhodkin N, Kulish N, Rodionova T (2013) Faceting of twin tips in polysilicon films. *J Cryst Growth* 381:65
128. Chen J, Bere A, Nouet G, Ruterana P (2004) Analysis of faceting of grain boundaries in GaN. *Superlattices Microstruct* 36:369
129. Kim YJ, Blum ID, He J, Kantazidis MG, Dravid VP, Seidman DN (2014) Three-dimensional atom-probe tomographic analyses of lead-telluride based thermoelectric materials. *JOM* 66:2288
130. Kumar AKN, Watabe M, Kurokawa K (2013) Effect of boron on the microstructure of spark plasma sintered ultrafine WC. *Vacuum* 88:88
131. Yoshino T, Price JD, Wark DA, Watson EB (2006) Effect of faceting on pore geometry in texturally equilibrated rocks: implications for low permeability at low porosity. *Contrib Mineral Petrol* 152:169
132. Chatain D, Rabkin E, Derenne J, Bernardini J (2001) Role of the solid/liquid interface faceting in rapid penetration of a liquid phase along grain boundaries. *Acta Mater* 49:1123
133. Blum B, Menyhard M, Luzzi DE, McMahon CJ Jr (1990) TEM investigation of bismuth induced faceting of $\Sigma 3$ and near- $\Sigma 3$ grain boundaries in copper. *Scr Metall Mater* 24:169
134. Siegl R, Vitek V, Luzzi DE, Yan M (1997) Phase stability and grain boundary structure in the Cu-Bi system. *J Phase Equilib* 18:562
135. Loier C, Boos JY (1981) Striation and faceting of grain boundaries in nickel due to sulphur and other elements. *Metall Trans A* 12:129
136. Sarnelli E, Adamo M, Nappi C, Braccini V, Kawale S, Bellingeri E, Ferdeghini C (2014) Properties of high-angle Fe(Se, Te) bicrystal grain boundary junctions. *Appl Phys Lett* 104:162601
137. Menyhard M, Rothman B, McMahon CJ Jr (1993) Observation of segregation and grain boundary faceting by tellurium and oxygen in iron. *Scr Metall Mater* 29:1005
138. Straumal BB, Polyakov SA, Bischoff E, Gust W, Baretzky B (2005) Faceting of $\Sigma 3$ and $\Sigma 9$ grain boundaries in Cu-Bi alloys. *Acta Mater* 53:247
139. Kundu A, Asl KM, Luo J, Harmer M (2013) Identification of a bilayer grain boundary complex in Bi-doped Cu. *Scr Mater* 68:146
140. Donald AM, Brown LM (1979) Grain boundary faceting in Cu-Bi alloys. *Acta Metall* 27:59
141. Michael JR, Williams DB (1984) An analytical electron-microscopy study of the kinetics of the equilibrium segregation of bismuth in copper. *Metall Trans A* 15:99

142. Gokon N, Kajihara M (2008) Occurrence of faceting for [110] symmetric tilt boundaries in Cu doped with Bi. *Mater Trans* 49:2584
143. Yoshino T, Takei Y, Wark DA, Bruce Watson E (2005) Grain boundary wetness of texturally equilibrated rocks, with implications for seismic properties of the upper mantle. *J Geophys Res* 110:B08205
144. Yu Z, Wu Q, Rickman JM, Chan HM, Harmer MP (2013) Atomic-resolution observation of Hf-doped alumina grain boundaries. *Scr Mater* 68:703
145. Straumal BB, Kogtenkova O, Zieba P (2008) Wetting transition of grain boundary triple junctions. *Acta Mater* 56:925
146. Straumal BB, Baretzky B, Kogtenkova OA, Straumal AB, Sidorenko AS (2010) Wetting of grain boundaries in Al by the solid Al_3Mg_2 phase. *J Mater Sci* 45:2057. doi:10.1007/s10853-009-4014-6
147. Virtanen P, Tiainen T, Lepisto T (1998) Precipitation at faceting grain boundaries of Cu-Ni-Sn alloys. *Mater Sci Eng A* 251:269
148. Straumal B, Muschik T, Gust W, Predel B (1992) The wetting transition in high and low energy grain boundaries in the Cu(In) system. *Acta Metall Mater* 40:939
149. Vasiliev AL, Stepantsov EA, Roddatis VV, Kiselev NA, Olsson E, Ivanov ZG, Claeson T (1995) The structure of artificial grain boundaries in yttrium-stabilized ZrO_2 bicrystals with intermediate layers. *Phys Status Solidi A* 151:151
150. Read WT, Shokley W (1950) Dislocation models of crystal grain boundaries. *Phys Rev* 78:275
151. Kirch DM, Jannot E, Barrales-Mora LA, Molodov DA, Gottstein G (2008) Inclination dependence of grain boundary energy and its impact on the faceting and kinetics of tilt grain boundaries in aluminum. *Acta Mater* 56:4998
152. Brandenburg JE, Barrales-Mora LA, Molodov DA, Gottstein G (2013) Effect of inclination dependence of grain boundary energy on the mobility of tilt and non-tilt low-angle grain boundaries. *Scr Mater* 68:980
153. Brandenburg JE, Barrales-Mora LA, Molodov DA (2014) On migration and faceting of low-angle grain boundaries: experimental and computational study. *Acta Mater* 77:294
154. Kirch DM, Zhao B, Molodov DA (2007) Faceting of low-angle $\langle 100 \rangle$ tilt grain boundaries in aluminum. *Scr Mater* 56:939
155. Grange G, Jourdan C, Gastaldi J (1988) Formation of grain boundary faceting during growth of Al crystals from melt. *J Cryst Growth* 87:325
156. Sandiumenge F, Vilalta N, Rabier J, Obradors X (2001) Sub-grain boundary structure in melt-textured $\text{RBa}_2\text{Cu}_3\text{O}_7$ (R = Y, Nd): limitation of critical currents versus flux pinning. *Phys Rev B* 64:184515
157. Yan Y, Evetts JE, Soyul B, Stobbs WM (1994) The compositionally modulated faceting of grain boundaries in the $\text{Bi}_2\text{Sr}_2\text{Ca}_{N-1}\text{Cu}_N\text{O}_x$ system. *Philos Mag Lett* 70:195
158. Song X (2005) (110) facets and dislocation structure of low-angle grain boundaries in $\text{YBa}_2\text{Cu}_3\text{O}_{7-\delta}$ and $\text{Y}_{0.7}\text{Ca}_{0.3}\text{Ba}_2\text{Cu}_3\text{O}_{7-\delta}$ thin film bicrystals. *J Mater Res* 22:950
159. Rollett AD, Srolovotz DJ, Doherty RD, Anderson MP (1989) Computer simulation of recrystallization in non-uniformly deformed metals. *Acta Metall* 37:627
160. Straumal B, Sursaeva V, Risser S, Chenal B, Gust W (1996) The onset of abnormal grain growth in Al-Ga polycrystals. *Mater Sci Forum* 207:557
161. Harper JME, Cabral C Jr, Andricacos PC, Gignac L, Noyan IC, Rodbell KP, Hu CK (1999) Mechanisms for microstructure evolution in electroplated copper thin films near room temperature. *J Appl Phys* 86:2516
162. Huda Z (2004) Influence of particle mechanisms on kinetics of grain growth in a P/M superalloy. *Mater Sci Forum* 467:985
163. Rabkin E (1998) Zener drag in the case of anisotropic grain boundary energy. *Scr Mater* 39:1631
164. Zener C (1948) Grains, phases, interfaces: an interpretation of microstructure. *Trans AIME* 175:15
165. Hibbard GD, McCrea JL, Palumbo G, Aust KT, Erb U (2002) An initial analysis of mechanisms leading to late stage abnormal grain growth in nanocrystalline Ni. *Scr Mater* 47:83
166. Lee H-Y, Freer R (1997) The mechanism of abnormal grain growth in $\text{Sr}_{0.6}\text{Ba}_{0.4}\text{Nb}_2\text{O}_6$ ceramics. *J Appl Phys* 81:376
167. Pang XM, Qiu JH, Zhu KJ, Luo J (2011) Study on the sintering mechanism of KNN-based lead-free piezoelectric ceramics. *J Mater Sci* 46:2345. doi:10.1007/s10853-010-5080-5
168. Kwon O-S, Hong S-H, Lee J-H, Chung U-J, Kim D-Y, Hwang NM (2002) Microstructural evolution during sintering of $\text{TiO}_2/\text{SiO}_2$ -doped alumina: mechanism of anisotropic abnormal grain growth. *Acta Mater* 50:4865
169. Dillon SJ, Harmer MP (2007) Mechanism of ‘‘solid-state’’ single-crystal conversion in alumina. *J Am Ceram Soc* 90:993
170. Dillon SJ, Harmer MP, Rohrer GS (2010) Influence of interface energies on solute partitioning mechanisms in doped aluminas. *Acta Mater* 58:5097
171. Fang T-T, Shiau H-K (2004) Mechanism for developing the boundary barrier layers of $\text{CaCu}_3\text{Ti}_4\text{O}_{12}$. *J Am Ceram Soc* 87:2072
172. Ryoo HS, Hwang SK (1998) Anisotropic atomic packing model for abnormal grain growth mechanism of WC-25 wt% Co alloy. *Scr Mater* 39:1577
173. Shin T-J, Oh J-O, Oh KH, Lee DN (2004) The mechanism of abnormal grain growth in polycrystalline diamond during high pressure-high temperature sintering. *Diam Relat Mater* 13:488
174. Lee SB, Hwang NM, Yoon DY, Henry MF (2000) Grain boundary faceting and abnormal grain growth in nickel. *Metall Mater Trans A* 31:985
175. Jung SH, Yoon DY, Kang SJL (2013) Mechanism of abnormal grain growth in ultrafine-grained nickel. *Acta Mater* 61:5685
176. Koo JB, Yoon DY (2001) The dependence of normal and abnormal grain growth in silver on annealing temperature and atmosphere. *Metall Mater Trans A* 32:469
177. Choi JS, Yoon DY (2001) The temperature dependence of abnormal grain growth and grain boundary faceting in 316L stainless steel. *ISIJ Int* 41:478
178. Shirdel M, Mirzadeh H, Parsa MH (2014) Microstructural evolution during normal/abnormal grain growth in austenitic stainless steel. *Metall Mater Trans A* 45:5185
179. Shirdel M, Mirzadeh H, Parsa MH (2014) Abnormal grain growth in AISI 304L stainless steel. *Mater Charact* 97:11
180. Choi JS, Yoon DY (2003) Temperature dependence of grain boundary structure and grain growth in bulk silicon-iron. *ISIJ Int* 43:245
181. Lee BK, Chung SY, Kang SJL (2000) Grain boundary faceting and abnormal grain growth in BaTiO_3 . *Acta Mater* 48:1575
182. An SM, Kang SJL (2011) Boundary structural transition and grain growth behavior in BaTiO_3 with Nd_2O_3 doping and oxygen partial pressure change. *Acta Mater* 59:1964
183. Cho YK, Yoon DY (2004) Faceting of high-angle grain boundaries in titanium-excess BaTiO_3 . *J Am Ceram Soc* 87:438
184. Lee SB, Sigle W, Ruhle M (2002) Investigation of grain boundaries in abnormal grain growth structure of TiO_2 -excess BaTiO_3 by TEM and EELS analysis. *Acta Mater* 50:2151
185. King AH (1998) Equilibrium at triple junctions under the influence of anisotropic grain boundary energy. In: Weiland H, Adams BL, Rollett AD (eds) Grain growth in polycrystalline materials III. TMS, Warrendale, pp 333–338
186. Gleiter H (1969) The mechanism of grain boundary migration. *Acta Metall* 17:565

187. Cahn JW (1960) Theory of crystal growth and interface motion in crystalline materials. *Acta Metall* 8:554
188. Heo YH, Jeon SC, Fisher JG, Choi SY, Hur KH, Kang SJL (2011) Effect of step free energy on delayed abnormal grain growth in a liquid phase-sintered BaTiO₃ model system. *J Eur Ceram Soc* 31:755
189. Viswanathan R, Bauer CL (1973) Formation of annealing twins, faceting and grain boundary pinning in copper bicrystals. *Mater Trans* 4:2645
190. Rabkin E (2005) Effect of grain boundary faceting on kinetics of grain growth and microstructure evolution. *J Mater Sci* 40:875. doi:10.1007/s10853-005-6504-5
191. Sursaeva VG, Gornakova AS, Yashnikov VP, Straumal BB (2008) Motion of the faceted 57° [112̄0] tilt grain boundary in zinc. *J Mater Sci* 43:3860. doi:10.1007/s10853-007-2223-4
192. Sursaeva VG (2010) Effect of faceting on twin grain boundary motion in zinc. *Mater Lett* 64:105
193. Barrett CD, El Kadiri H (2014) Fundamentals of mobile tilt grain boundary faceting. *Scr Mater* 84:15
194. Sursaeva VG, Gottstein G, Shvindlerman LS (2011) Effect of a first-order ridge on grain boundary motion in Zn. *Acta Mater* 59:623
195. Paidar V, Lejcek P, Polcarová M, Brádlér J, Jacques A (2004) Anisotropy of grain boundary migration observed in situ by synchrotron radiation. *Mater Sci Forum* 467:911
196. Sursaeva VG, Straumal BB, Gornakova AS, Shvindlerman LS, Gottstein G (2008) Effect of faceting on grain boundary motion. *Acta Mater* 56:2726
197. Straumal BB, Sursaeva VG, Gornakova AS (2005) Influence of faceting-roughening on the triple junction migration in zinc. *Zt Metallkd* 96:1147
198. Bonzel HP, Emundts A (2000) Absolute values of surface and step free energies from equilibrium crystal shapes. *Phys Rev Lett* 84:5804
199. Hondoh T, Higashi A (1979) Anisotropy of migration and faceting of large-angle grain boundaries in ice bicrystals. *Philos Mag A* 39:137
200. An SM, Yoon BK, Chung SY, Kang SJL (2012) Nonlinear driving force-velocity relationship for the migration of faceted boundaries. *Acta Mater* 60:4531
201. Minkwitz C, Chr Herzig, Rabkin E, Gust W (1999) The inclination dependence of gold tracer diffusion along a Σ3 twin grain boundary in copper. *Acta Mater* 47:1231
202. Klinger L, Rabkin E (2010) Sintering of fully faceted crystalline particles. *Int J Mater Res* 101:75
203. Lee MG, Chung SY, Kang SJL (2011) Boundary faceting-dependent densification in a BaTiO₃ model system. *Acta Mater* 59:692
204. James MN (2010) Intergranular crack paths during fatigue in interstitial-free steels. *Eng Fract Mech* 77:1998
205. Beachem CD (1972) A new model for hydrogen-assisted cracking (hydrogen “embrittlement”). *Metall Trans* 3:437
206. Hull D, Bacon DJ (1984) Introduction to dislocations. Pergamon Press, Oxford
207. Lee SB, Sigle W, Kurtz W, Rühle M (2003) Temperature dependence of faceting in Σ5 (310)[001] grain boundary of SrTiO₃. *Acta Mater* 51:975
208. Lee SB (2003) Correlation between grain boundary faceting-defaceting transition and change of grain boundary properties with temperature. *Mater Lett* 57:3779
209. Lee SB, Sigle W, Rühle M (2003) Faceting behavior of an asymmetric SrTiO₃ Σ5 [001] tilt grain boundary close to its defaceting transition. *Acta Mater* 51:4583
210. Lee SB, Lee JH, Cho PS, Sigle W, Phillipp F (2007) High-temperature resistance anomaly at a strontium titanate grain boundary and its correlation with the grain-boundary faceting-defaceting transition. *Adv Mater* 19:391
211. Hartmann K, Wirth R, Heinrich W (2010) Synthetic near Σ5 (210)[100] grain boundary in YAG fabricated by direct bonding: structure and stability. *Phys Chem Miner* 37:291
212. Jin Q, Chan SW (2002) Grain boundary faceting in YBa₂Cu₃O_{7-x} bicrystal thin films on SrTiO₃ substrates. *J Mater Res* 17:323
213. Eastman JA, Vaudin MD, Merkle KL, Sass SL (1989) Electron diffraction study of the faceting of tilt grain boundaries in NiO. *Philos Mag A* 59:465
214. Ekin JW, Braginski AI, Panson AJ, Janocko MA, Capone DW II, Zaluzec NJ, Flandermeyer B, de Lima OF, Hong M, Kwo J, Liou SH (1987) Evidence for weak link and anisotropy limitations on the transport critical current in bulk polycrystalline YBa₂Cu₃O_x. *J Appl Phys* 62:4821
215. Dimos D, Chaudhari P, Mannhart J (1990) Superconducting transport properties of grain boundaries in YBa₂Cu₃O₇ bicrystals. *Phys Rev B* 41:4038
216. Hilgenkamp H, Mannhart J, Mayer B (1996) Implications of $d(x^2-y^2)$ symmetry and faceting for the transport properties of grain boundaries in high- T_c superconductors. *Phys Rev B* 53:14586
217. Browning ND, Buban JP, Nellist PD, Norton DP, Chisholm MF, Pennycook SJ (1998) The atomic origins of reduced critical currents at [001] tilt grain boundaries in YBa₂Cu₃O_{7-δ} thin films. *Phys C* 294:183
218. Tsai JWH, Chan SW, Kirtley JR, Tidrow SC, Jiang Q (2001) The variation of J_{cgb} with GB misorientation and inclination measured using the scanning SQUID microscope. *IEEE Trans Appl Supercond* 11:3880
219. Sandiumenge F, Vilalta N, Rabier J, Obradors X (2002) Sub-boundary mesostructures and variable dislocation networks in single domain melt textured YBa₂Cu₃O₇—implications on critical currents. *J Phys C* 372:1204
220. Laval JY, Swiatnicki W (1994) Atomic structure of grain boundaries in YBa₂Cu₃O_{7-x}. *Phys C* 221:11
221. Lombardi F, Tafuri F, Ricci F, Miletto Granozio F, Barone A, Testa G, Sarnelli E, Kirtley JR, Tsuei CC (2002) Intrinsic d -wave effects in YBa₂Cu₃O_{7-δ} grain boundary Josephson junctions. *Phys Rev Lett* 89:207001
222. Mitchell EE, Foley CP (2011) YBCO step-edge junctions: influence of morphology on junction transport. *IEEE Trans Appl Supercond* 21:371
223. Lombardi F, Tafuri F, Ricci F, Miletto F, di Uccio US, Testa G, Sarnelli E (2002) Influence of the structural anisotropy and of the order parameter symmetry on the transport properties of YBa₂Cu₃O_{7-δ} grain boundaries Josephson junctions. *Phys C* 372:87
224. Chisholm MF, Smith DA (1989) Low-angle tilt grain boundaries in YBa₂Cu₃O₇ superconductors. *Philos Mag A* 59:181
225. Yan Y, Evetts JE, Soyly B, Stobbs WM (1996) The origins of high values of the critical current density in the Bi₂Sr₂Ca_{n-1}Cu_nO_x system: high- T_c superconducting pathways at low angle tilt boundaries. *Phys C* 261:56
226. Yan Y, Kirk MA, Evetts JE (1997) Structure of grain boundaries: correlation to supercurrent transport in textured Bi₂Sr₂Ca_{n-1}Cu_nO_x bulk material. *J Mater Res* 12:3009
227. Shadrin P, Jia CL, Divin Y (2003) Spread of critical currents in thin-film YBa₂Cu₃O_{7-x} bicrystal junctions and faceting of grain boundary. *IEEE Trans Appl Supercond* 13:603
228. Shadrin P, Jia CL, Divin Y (2002) Spread of critical currents in thin-film YBa₂Cu₃O_{7-x} bicrystal junctions and faceting of grain boundary. *Phys C* 372:80

229. Borisenko IV, Constantinian KY, Kisilinskii YV, Ovsyannikov GA (2004) Andreev states and shot noise in bicrystal junctions of cuprate superconductors. *JETP* 99:1223
230. Deutscher G (1989) Superconductivity in the high- T_c oxides. *Phys Scr* 29:9
231. Camps RA, Evetts JE, Glowacki BA, Newcomb SB, Stobbs WM (1987) Microstructure and critical current of superconducting $\text{YBa}_2\text{Cu}_3\text{O}_{7-x}$. *J Mater Res* 2:750
232. Blendell JE, Handwerker CA, Vaudin MD, Fuller ER Jr (1988) Composition control of the microstructure of $\text{Ba}_2\text{YCu}_3\text{O}_{6+x}$. *J Cryst Growth* 89:93
233. Zandbergen HW, Thomas G (1988) Grain boundaries in sintered $\text{YBa}_2\text{Cu}_3\text{O}_{7-\delta}$. *Acta Crystallogr A* 44:772
234. Kogure T, Zhang Y, Levonmaa R, Kontra R, Wang WX, Rudman DA, Yurek GJ, van der Sande JB (1988) Grain boundary structure of $\text{YBa}_2\text{Cu}_3\text{O}_{7-x}$ formed by oxidation of metallic precursors. *Phys C* 156:707
235. Romano LT, Wilshaw PR, Long NJ, Grovenor CRM (1989) High-resolution microchemistry and structure of grain boundaries in bulk $\text{YBa}_2\text{Cu}_3\text{O}_{7-x}$. *Supercond Sci Technol* 1:285
236. Babcock SE, Larbalestier DC (1989) Evidence for local composition variations within $\text{YBa}_2\text{Cu}_3\text{O}_{7-\delta}$ grain boundaries. *Appl Phys Lett* 55:393
237. Gao Y, Merkle K, Bai G, Chang HLM, Lain DJ (1991) Structure and composition of grain boundary dislocation cores and stacking faults in MOCVD-grown $\text{YBa}_2\text{Cu}_3\text{O}_{7-x}$ thin films. *Phys C* 174:1
238. Carim AH, Mitchell TE (1993) 90-degree boundaries and associated interfacial and stand-off partial dislocations in $\text{Ba}_2\text{Cu}_3\text{O}_{7-x}$. *Ultramicroscopy* 51:228
239. Hilgenkamp H, Mannhart J, Mayer B, Gerber Ch, Kirtley JR, Moler KA (1997) Influence of $d(x^2-y^2)$ symmetry on device applications of high- T_c grain boundary junctions. *IEEE Trans Appl Supercond* 7:3670
240. Mannhart J, Hilgenkamp H, Mayer B, Kirtley JR, Moler KA, Sigrist M (1996) Large enhancement of critical-current density due to vortex matching at the periodic facet structure in $\text{YBa}_2\text{Cu}_3\text{O}_{7-\delta}$ bicrystals. *Phys Rev Lett* 77:2782
241. Mints RG, Papiashvili I, Kirtley JR, Hilgenkamp H, Hammerl G, Mannhart J (2002) Observation of splintered Josephson vortices at grain boundaries in $\text{YBa}_2\text{Cu}_3\text{O}_{7-\delta}$. *Phys Rev Lett* 89:067004
242. Cai XY, Gurevich A, Tsu IF, Kaiser DL, Babcock SE, Larbalestier DC (1998) Large enhancement of critical-current density due to vortex matching at the periodic facet structure in $\text{YBa}_2\text{Cu}_3\text{O}_{7-\delta}$ bicrystals. *Phys Rev B* 57:10951
243. Walker MB (1996) Mechanism for magnetic-flux generation in grain boundaries of $\text{YBa}_2\text{Cu}_3\text{O}_{7-x}$. *Phys Rev B* 54:13269